On the model of equatorial Magnetic-Archimedes-Coriolis waves propagating at Earth's core surface and the potential implications

Pengshuo Duan[1], Chengli Huang[2], and Cancan Xu[3]

[1]Shanghai Astronomical Observatory, Chinese Academy of Sciences
[2]Shanghai Astronomical Observatory (CAS)
[3]Shanghai Astronomical Observatory

November 23, 2022

Abstract

The purposes of this work are (1) clarifying the specific latitude range in which the currently physical model of the equatorial trapped Magnetic-Archimedes-Coriolis (namely eMAC) waves propagating atop the Earth's core can own the enough accuracy to describe the hydromagnetic waves; (2) presenting the systematically analytical expressions to represent the physical properties (e.g., the equatorial confinement and latitudinal distribution, damping rate α, eigen-period T) of the eMAC waves. Here, the new results indicate that: 1) the eMAC wave model can own the high accuracy (i.e., the relative errors are less than 5%) to describe the core waves in the regions with latitude below 25 degrees ; 2) the equatorial confinement and latitudinal distribution law is essentially governed by a specific solution form with the typical Hermite polynomial term of degree n; 3) the damping rate can be estimated by α [?]-pˆ2/($\mu\sigma$Hˆ2) (μ being the vacuum permeability, σ being the core electrical conductivity; H being the stratified layer thickness of the core), showing that the magnetic diffusivity η (=1/($\mu\sigma$))can cause the ohmic dissipation of the waves; besides, the H value is predicted to be larger than 20km, when T matches the observed 8.5yr period. This work also presents the analytical models for the perturbed magnetic fields due to the eMAC waves, presenting that the azimuthal perturbed magnetic field bφ(with degree n=1) is mainly confined to the equatorial regions with latitude below ˜15 degrees, the profile of which coincides with the observed core surface azimuthal flows.

On the model of equatorial Magnetic-Archimedes-Coriolis waves propagating at Earth's core surface and the potential implications

Pengshuo Duan[1*], Chengli Huang[1,2] and Cancan Xu[1,2]

[1]CAS Key Laboratory of Planetary Sciences, Shanghai Astronomical Observatory, Chinese Academy of Sciences, Shanghai 200030, China;

[2] School of Astronomy and Space Science, University of Chinese Academy of Sciences, Beijing 100049, China;

*Corresponding authors: P. Duan (duanps@shao.ac.cn).

Abstract

The purposes of this work are (1) clarifying the specific latitude range in which the currently physical model of the equatorial trapped Magnetic-Archimedes-Coriolis (namely eMAC) waves propagating atop the Earth's core can own the enough accuracy to describe the hydromagnetic waves; (2) presenting the systematically analytical expressions to represent the physical properties (e.g., the equatorial confinement and latitudinal distribution, damping rate α, eigen-period T) of the eMAC waves. Here, the new results indicate that: 1) the eMAC wave model can own the high accuracy (i.e., the relative errors are less than 5%) to describe the core waves in the regions with latitude below 25 degrees; 2) the equatorial confinement and latitudinal distribution law is essentially governed by a specific solution form with the typical Hermite polynomial term of degree n; 3) the damping rate can be estimated by $\alpha \approx -\frac{\pi^2}{\mu\sigma H^2}$ (μ being the vacuum permeability, σ being the core electrical conductivity, H being the stratified layer thickness of the core), showing that the magnetic diffusivity η ($=\frac{1}{\mu\sigma}$) can cause the ohmic dissipation of the waves; besides, the H value is predicted to be larger than 20km, when T matches the observed 8.5yr period. This work also presents the analytical models for the perturbated magnetic fields due to the eMAC waves, presenting that the azimuthal perturbed magnetic field b_φ (with degree n=1) is mainly confined to the equatorial regions with latitude below ~15 degrees, the profile of which coincides with the observed core surface azimuthal flows.

Plain language Summary

Modern observations show that the fast fluctuations in geomagnetic acceleration and fluid core surface flow motions always occur at the equatorial regions, which may arise from the rapidly hydromagnetic waves atop the Earth's core. But, the exact origins of these waves are still unclear, though the so-called eMAC waves may provide a potential mechanism. Given that the physical expressions of describing the physical properties (e.g., equatorial confinement and latitudinal distribution, damping rate, eigen-period) and the perturbed magnetic fields of the eMAC waves have not been given before, this work carefully revisits the currently eMAC wave theory and firstly gives the systematically analytical expressions for these physical properties. Importantly, the perturbation analysis indicates that the eMAC wave model can own the high accuracy (i.e., the relative errors are less than 5%) to describe the low-latitude waves with latitude below 25 degrees, which can cover the regions where the observed equatorial waves mainly locate. In summary, this work provides an important complement for the currently eMAC wave theory. The results of this work are significant to understand the physical mechanism responsible for the origins of the observed equatorial waves, their physical properties and the dynamics of the Earth's equatorial regions.

Key points:

1. The systematically analytical expressions about the physical properties of the eMAC waves are given.
2. Relative errors of the eMAC wave model in describing the hydromagnetic waves with the latitude below 25 degrees are less than 5%.
3. Discussed implications of the eMAC wave model to the core stratification and equatorial region dynamics.

1. Introduction

Many recent works (e.g., Gillet et al, 2015; Chulliat et al, 2015; Finlay et al, 2016; Kloss and Finlay, 2019) showed that the Earth equatorial region is a place of presenting vigorously localized interannual alternating fluid motions, which reflects the short-period fluctuations in geomagnetic acceleration. For example, Gillet et al (2015) found that the strongly interannual time-dependent

azimuthal fluid outer core (FOC) flows occur at the equatorial region with latitude below 10 degrees; Finlay et al (2016) showed that the observed pulses in geomagnetic acceleration mainly locate below the India Ocean between the equator and 30°S from the CHAOS-6 model, while Kloss and Finlay (2019) presented a new model of time-dependent core flow derived from geomagnetic measurements by Swarm and CHAMP satellites and ground observatories, which further confirmed the equatorially confined phenomena (within latitudes ~15°N and S) of the non-zonal azimuthal core flows and geomagnetic acceleration pulses. Nevertheless, the issue why these azimuthal flows and geomagnetic acceleration signals perform the equatorially trapped behaviors and show the generally short-lived features is less clear (e.g., Gillet et al, 2015; Finlay et al, 2016; Buffett and Matsui, 2019).

Additionally, Chi-Durán et al (2020) suggested that these observed geomagnetic acceleration signatures may result from the superposition of FOC flows with different frequency components, and they detected two fluid core traveling waves with ~8.7yr and ~7.08yr periods on the subdecadal (i.e., 5~10yr) scales, which respectively occur at southeast Asia and Atlantic equatorial regions, where the propagation direction of the former is eastward, while the latter is westward. Any further advance of better understanding the physics of the origins of these periodic equatorial waves is vital, while it is also interesting to explore the physical mechanisms responsible for these two periodic waves, as length of day (LOD) changes also have the same two periodic components, i.e., the ~8.6yr and ~7.2yr period signals (Duan and Huang, 2020; Hsu et al, 2021), which are shown to be unrelated to the Earth surface factors (e.g., AAM/OAM/HAM) (Hsu et al, 2021). Moreover, Duan and Huang (2020) showed that there is a good correspondence between the extremes of the ~8.6yr oscillation in LOD and the occurrence epochs of the geomagnetic field fast changes (i.e., geomagnetic jerks), which means that this ~8.6yr signal and the jerks may originate from a same physical source, i.e., the fast equatorial waves with subdecadal periods propagating at the core surface, since many works (e.g., Wardinski et al, 2008; Mandea et al, 2010; Chulliat et al, 2010; Chulliat and Maus, 2014; Kloss and Finlay, 2019; Aubert and Finlay, 2019) showed that the equatorial waves propagating at the core surface closely correlate with the geomagnetic jerks.

However, the precise mechanisms responsible for these equatorial waves are still unclear, though they may reflect a type of fluid core surface waves, i.e., the so-called equatorial Magnetic-Archimedes-Coriolis (eMAC) waves (e.g., Buffett and Matsui, 2019), for example, the

origin of the ~8.6yr periodic equatorial waves was suggested to be attributed to the eMAC wave mechanism (Chi-Durán et al, 2020), where a strong gradient in the magnetic force at the core-mantle boundary (CMB) away from the equator can produce the so-called wave guide to cause the equatorially trapped features for the MAC waves (Buffett and Matsui, 2019). Of course, these observed equatorial waves may also be related to the quasi-geostrophic Alfvén waves (e.g., Finlay et al, 2010; Gillet et al, 2012; Teed et al, 2019; Aubert and Finlay, 2019) or the Magneto-Coriolis (MC) modes within FOC on the subdecadal scales (Gerick et al, 2020), for example, Gillet et al (2022) recently also detected the ~7yr periodic magnetic waves in the Earth's core from the Satellite data and they interpretated the ~7yr waves as the signatures of MC modes.

Given that the eMAC waves differ from the MC modes, for example, the former only emerges inside a stratified layer at the FOC surface (Buffett and Matsui, 2019), while the latter happens in the FOC without requiring the core stratification (Gerick et al, 2020), but interestingly, both of which can present the same physical properties (with interannual changes) localized near the equator similar to the observations (e.g., Finlay and Jackson, 2003; Finlay et al, 2016). Therefore, it is necessary to further clarify the differences between these two modes to explain the origins of these observed fast equatorial waves with the subdecadal periods, while this work will mainly focus on the eMAC wave mechanism.

Up to now, many efforts (e.g., Knezek and Buffett, 2018, 2019; Buffett and Matsui 2019) have been made to study the origins of short-period equatorial waves propagating at the core surface from the perspective of MAC waves. According to the spatial distribution features of these observed equatorial waves, Knezek and Buffett (2019) suggested that these waves can be fitted by a selected Hermite polynomial basis functions of degree n, nevertheless, at that time, they did not give the rigorous theory basis to prove that why the so-called Hermite polynomial functions can feature these waves. Through considering the different physical influences (e.g., the spherical geometry, gradients in the radial magnetic field) and focusing on the low-latitude regions, Buffett and Matsui (2019) (hereafter BM19) developed a physical model for the equatorial trapped MAC waves (namely eMAC waves), in particular, they derived a type of second-order differential equation (see their equations (25), (35), (41) or (46), all of which have the same mathematical form, which is called as the 'Weber equation' in physics) to describe the perturbed magnetic field changes with the latitude, while they referred to a specific solution form with the term of

aforementioned Hermite polynomial of degree n (see the equation (27) in BM19).

It should be noted that, the process of deriving the above 'Weber equation' involves the truncation treatment (that is, removing the relevantly higher-order terms, which depend on the latitude) and this treatment may cause the significant truncation errors for the model results locating at the high-latitude regions. However, the specific latitude range in which the 'Weber equation' can own the enough accuracy to describe the perturbed magnetic fields is still less clear. Besides, BM19 mainly focused on the numerical discussion of the above differential equation and its solution, but they did not give the subsequently analytical expressions to represent the physical properties (e.g., the equatorial confinement and latitudinal distribution, damping rate, eigen-period, propagating velocity) of the waves. The detailed physical factors that can influence these properties are also still less clear.

On the basis of the previous work (i.e., BM19) about the eMAC wave theory, this work will further carefully derive the aforementioned differential equation (i.e., the so-called 'Weber equation') and discuss its specific solution in an analytical approach as well as making the perturbation analysis to determine the latitude range of the 'Weber equation' and its specific solution owning the enough accuracy. One of the objectives of this work is to give the systematically analytical expressions of representing the physical properties of the eMAC waves, from which, not only can we show that the equatorial confinement and latitudinal distribution features of the MAC waves are essentially governed by the specific solution with the Hermite polynomial term of degree n, but also can clearly show the physical factors that determine the related properties of the waves. Importantly, the perturbation analysis indicates that the related results of this work can own the high accuracy (i.e., the relative errors are shown to be less than 5%) to describe the hydromagnetic waves in the regions with latitude below 25 degrees, which can cover the region where the observed equatorial waves mainly locate (e.g., Gillet et al, 2015; Chulliat et al, 2015; Kloss and Finlay, 2019). Therefore, the results of this work are significant to understand the origins of the observed equatorial waves and their physical properties.

Finally, we discuss the possible stratification parameters inferred by the eMAC waves, the equatorial confinement degree influenced by the strength of the radial magnetic field at the CMB equator and the physical possibility of the eMAC waves carrying the axial angular momentum.

2. Theory part

2.1. On the theory of MAC waves

Previous works (e.g., Bergman, 1993; Braginsky, 1993) indicated that if a stable stratified layer exists at the Earth's core surface, the interaction of Coriolis-Lorentz-Buoyancy forces inside this layer will enable a type of hydromagnetic waves, i.e., the so-called Magnetic-Archimedes-Coriolis (MAC) waves. That is to say, the existence of these MAC waves requires a stable stratified layer, which is characterized by the stratification parameters (the related parameters used in this work are listed in Table 1), i.e., the thickness *H* and the stratification degree *N*. Here, *N* is called as the buoyancy (or Brunt-Väisälä) frequency, which is expressed by

$$N = \sqrt{-\frac{g}{\rho_0}\frac{\partial \rho_0}{\partial r}} \tag{1}$$

where, g is the acceleration due to gravity; ρ_0 is the density of the fluid core, $\frac{\partial \rho_0}{\partial r}$ refers to the radial derivative.

Furthermore, many works from seismic wave observations, geochemistry and geomagnetism (e.g., Helffrich and Kaneshima, 2010; Buffett and Seagle, 2010; Gubbins and Davies, 2013; Buffett, 2014) supported that there is a strongly stratified layer existing at the core surface. In particular, some works (e.g., Gubbins and Davies, 2013; Helffrich and Kaneshima, 2010) provided the valuable information about the parameters of *H* and *N*. For example, Gubbins and Davies (2013) indicated that the thickness (*H*) of the stratified layer is ~100km or less, which is due to the barodiffusion of the light elements; while Helffrich and Kaneshima (2010) showed a strong density stratified layer with the buoyancy periods of 1.63~3.43h (corresponding to 7Ω~15Ω, Ω being the rotation rate) existing at the core surface from the observed core wave speed profile, though the issue that whether a stable stratification layer exists atop the Earth's core is still debated (e.g., Gastine et al, 2019), where, the exact *H* and *N* values are still highly uncertain.

In order to further explore the potential physical origins of the observed equatorial hydromagnetic waves from the eMAC wave mechanism, as in previous studies, this work still adopts the assumption that a stable stratification layer exists atop the Earth's core. Meanwhile, considering the uncertainties of the stratification parameters, this work takes the values of *H* and *N* as the variables (see Table 1).

Table 1 Parameters used in this work.

Parameter	Symbol	Value
Fluid core density	ρ_0	1.1×10^4kgm^{-3}
Earth's rotation velocity	Ω	7.272×10^{-5}rad/s
Vacuum permeability	μ	$4\pi\times10^{-7}$H/m
Radius of the CMB	R	3.48×10^6m
Electrical conductivity at the core surface [a]	σ	10^6S/m
Radial magnetic field at CMB equator [b]	$B_r(0)$	0.48mT
Strength of the magnetic gradients at CMB [b]	β	$1.58(\approx\sqrt{2.5})$
Space wave number [c]	m	7
Buoyancy frequency [d]	N	7Ω to 15Ω
Thickness of the stratified layer	H	10 to 100 km

a refers to Ohta et al (2016); b refers to Buffett and Matsui (2019); c shows Chi-Durán et al (2020); d indicates Helffrich and Kaneshima (2010).

Here, firstly let's revisit the previous work (i.e., BM19) about the eMAC wave theory. If the fluid core is stratified, then the vertical fluid motions can disturb the density field, causing the pressure perturbation and the large-scale horizontal flows, where the hydromagnetic waves can be treated as the small perturbation with respect to the background state, where, the background state is defined by velocity $\vec{V}_0$, magnetic field $\vec{B}_0$, pressure P_0 and density ρ_0. Considering the non-linear terms exist, for example, the Lorentz force term has the general form $\vec{B}_0\cdot\nabla\vec{b}+\vec{b}\cdot\nabla\vec{B}_0$, here, the vertical length scale H (<100km) is much smaller than the horizontal scale (L~3000km), so the latter term (i.e., $\vec{b}\cdot\nabla\vec{B}_0$) can be much weaker than the first term ($\vec{B}_0\cdot\nabla\vec{b}$), thus, a linearized momentum equation for perturbed terms with respect to a static background state is given by

$$\frac{\partial\vec{v}}{\partial t}+\underbrace{2\vec{\Omega}\times\vec{v}}_{\text{Coriolis force}}=-\frac{1}{\rho_0}\nabla p+\underbrace{\frac{1}{\rho_0\mu}\vec{B}_0\cdot\nabla\vec{b}}_{\text{Lorentz force}}+\underbrace{\frac{\rho_1}{\rho_0}\vec{g}}_{Buoyancy\ force} \tag{2}$$

where, $\vec{v}$ is the perturbed fluid core velocity resulting from the interplay of Coriolis-Lorentz-Buoyancy forces; $\vec{\Omega}$ is the Earth rotation angular velocity vector; $\vec{b}$ is called as the perturbed magnetic field; $\vec{g}=-g\vec{e}_r$ is the gravity acceleration vector, here $\vec{e}_r$ is the unit radial vector; p

is the perturbed pressure; μ is the vacuum permeability; ρ_1 is the perturbed density.

The fluid core inside the stratification layer is treated as the incompressible fluid and it satisfies the continuity condition, i.e., $\nabla \cdot \vec{v}$=0, which is described in the spherical coordinates (r, θ, φ), here θ, φ respectively refers to the co-latitude and longitude. Because of $H << R$ (here R is the CMB radius), so we have

$$\frac{\partial v_r}{\partial r} + \frac{1}{Rsin\theta}\frac{\partial}{\partial \theta}(v_\theta sin\theta) + \frac{1}{Rsin\theta}\frac{\partial v_\varphi}{\partial \varphi} = 0 \quad (3)$$

where, v_r, v_θ and v_φ respectively express the radial, latitudinal and azimuthal velocities.

Meanwhile, the incompressible fluid core respects the following mass conservation law

$$\frac{\partial \rho_1}{\partial t} = -v_r \frac{\partial \rho_0}{\partial r} \quad (4)$$

Here, we directly present the relationship between the perturbed magnetic field and the perturbed flow velocity within the stratification layer, which is expressed by (i.e., the equation (8) in BM19)

$$\frac{\partial \vec{b}_\zeta}{\partial t} = B_r \frac{\partial \vec{v}_\zeta}{\partial r} + \eta \frac{\partial^2 \vec{b}_\zeta}{\partial^2 r} \quad (5)$$

where, $\zeta = r, \theta, \varphi$; b_ζ refers to the perturbed magnetic field; v_ζ reflects the perturbed fluid core velocities; B_r signifies the radial component of the background magnetic field; $\eta(=\frac{1}{\mu\sigma})$ is the magnetic diffusivity, σ being the electrical conductivity at the core surface.

The above equations (i.e., (2), (3), (4) and (5)) represent the boundary conditions on the upper and lower surfaces of the stratified layer (see BM19), where, v_r is assumed to vanish at the CMB, i.e., $v_r = 0$, at $r = R$; because the horizontal fluid motions below the stratified layer are opposed by the magnetic friction effects, so the horizontal perturbed velocities are considered to be stationary, that is, $v_\varphi = v_\theta = 0$ (at $r = R - H$); while $b_\theta = b_\varphi = 0$ at the CMB ($r = R$) is required by the pseudo-vacuum conditions.

Besides, to conveniently discuss the physical model of the MAC waves, BM19 further converted the above governing equations from the spherical coordinates (r, θ, φ) to the new coordinates (z, x, φ), here, $z = r - R$, x refers to a meridional coordinate (i.e., $x = cos\,\theta$), while they defined two new variables (i.e., b'_θ and b'_φ) for the perturbed magnetic fields (i.e., b_θ and b_φ), that is, $b'_\theta = \sqrt{1-x^2}\,b_\theta$ and $b'_\varphi = \frac{1}{\sqrt{1-x^2}}b_\varphi$. Given that the general expression of the travelling waves within the stratified layer can be written in the form of $f(\vec{X} - \vec{V}t)$, where, $\vec{X}$

being the position on the CMB, $\overrightarrow{V}$ being the wave propagating velocity, the so-called MAC waves must satisfy the typical wave equation, here the perturbed magnetic fields due to these MAC waves are expressed in the following form

$$\left.\begin{aligned} b'_\theta &= \tilde{b}'_\theta(x)\, sin(\, kz)\, exp[\, im(\varphi - \tilde{V}\tilde{t})] = \tilde{b}'_\theta(x)\, sin(\, kz)\, exp[\, i(m\varphi - \tilde{\omega}\tilde{t})] \\ b'_\varphi &= \tilde{b}'_\varphi(x)\, sin(\, kz)\, exp[\, im(\varphi - \tilde{V}\tilde{t})] = \tilde{b}'_\varphi(x)\, sin(\, kz)\, exp[\, i(m\varphi - \tilde{\omega}\tilde{t})] \end{aligned}\right\} \quad (6)$$

where, $\tilde{b}'_\theta(x)$ and $\tilde{b}'_\varphi(x)$ respectively express the amplitudes of the perturbed magnetic field, which also reflect the latitudinal distribution of the MAC waves; $\tilde{t} = t - t_0$, here t_0 is the initial time; the boundary condition of perturbed magnetic field requires $k = \frac{j\pi}{H}$, j (=1,2,⋯) is the vertical wave number; m is the space angular frequency or the space wave number; $i^2 = -1$; the complex frequency $\tilde{\omega}$ is written as $\tilde{\omega}$=$\omega + i\alpha$, here, ω being the temporal angular frequency (or the eigen-frequency), α being the damping rate, here $\alpha < 0$, meaning the typically exponential decaying oscillation mode; and $\tilde{\omega} = m\tilde{V}$, so $\tilde{V} = \frac{\tilde{\omega}}{m} = \frac{\omega}{m} + i\frac{\alpha}{m}$, defining $V = Re(\tilde{V}) = \frac{\omega}{m} = \frac{2\pi}{mT}$, here, V refers to the propagation velocity (i.e., phase speed), the sign of which determines the propagation direction, i.e., the sign '+' means eastward propagation, while '-' implies westward propagation; Re means to take the real part, T refers to the eigen-period.

2.2. Derivation of the 'Weber equation'

According to the above formulas (i.e., (1), (2), (3), (4), (5) and (6)), we show the following equation (i.e., the equations (16) and (17) in BM19)

$$\left.\begin{aligned} \partial_x^2\tilde{b}'_\theta - \tfrac{M-I}{1-x^2}\tilde{b}'_\theta &= Cxi\tilde{b}'_\varphi + im\partial_x\tilde{b}'_\varphi \\ [-m^2 - (M-I)(1-x^2)]\tilde{b}'_\varphi &= -Cxi\tilde{b}'_\theta + im\partial_x\tilde{b}'_\theta \end{aligned}\right\} \quad (7)$$

where, $C = \frac{2\Omega\tilde{\omega}k^2R^2}{N^2}$, $M = \frac{V_a^2k^4R^2}{\chi N^2}$, $I = \frac{\tilde{\omega}^2k^2R^2}{N^2}$, which respectively measure the importance of Coriolis force, Magnetic force and Inertia force with respect to the buoyancy force; here $V_a = \frac{B_r}{\sqrt{\rho_0\mu}}$ being the Alfvén wave velocity; $\chi = 1 + \frac{i\eta k^2}{\tilde{\omega}}$, showing the influence of magnetic diffusion.

On the subdecadal (i.e., 5~10yr) period scales, the inertia force term is shown to be much weaker than the magnetic force term, i.e., $I << M$ (see the discussion part). Removing the I term from formula (7), we obtain

$$\left.\begin{array}{c}\partial_x^2\tilde{b}'_\theta - \frac{M(x)}{1-x^2}\tilde{b}'_\theta = Cxi\tilde{b}'_\varphi + im\partial_x\tilde{b}'_\varphi \\ \tilde{b}'_\varphi = \frac{Cxi\tilde{b}'_\theta - im\partial_x\tilde{b}'_\theta}{m^2+(1-x^2)M(x)}\end{array}\right\} \quad (8)$$

where, $x = cos\,\theta$ and $|x| < 1$.

Here, we will present the expression of $M(x)$. Given that B_r at the CMB is not a constant value with respect to the latitude (e.g., Jackson, 2003; Christensen and Aubert, 2006), but its root-mean-square increases towards to the poles, BM19 further indicated that the large-scale trend of longitudinal averaged value B_r^2 can be generally approximated by a quadratic dependence on x, that is, $B_r^2 = B_r^2(0)(1+\beta^2x^2)$, where, $B_r(0)$ (~0.48mT, see Table 1) refers to the radial magnetic field strength at the CMB equator, the factor β (~1.58, see Table 1) is a fitting parameter, reflecting the gradient strength of the magnetic force over the CMB surface. Obviously, if $\beta = 0$, then $B_r(x) = B_r(0)$, in this case, B_r is a constant value regarding *x*. Thus, the $M(x)$ term can be expressed by

$$M(x) = M(0)(1+\beta^2x^2) \quad (9)$$

where, $M(0) = \frac{V_a\,(0)^2k^4R^2}{\chi N^2}$; $V_a(0) = \frac{B_r(0)}{\sqrt{\rho_0\mu}}$ being the Alfvén wave velocity at the CMB equator.

Furthermore, BM19 presented a second-order differential equation, i.e., formula (10) (see their equation (44)), which was suggested to be directly derived from the formula (8) after dropping the small terms with $\frac{|M(x)|}{m^2} \ll 1$.

$$(1-x^2)\partial_x^2\tilde{b}'_\theta - 2x(\frac{1-\beta^2+2\beta^2x^2}{1+\beta^2x^2})\partial_x\tilde{b}'_\theta + [\frac{C^2x^2}{M(x)} + \frac{mC}{M(x)} - \frac{m^2}{1-x^2}]\tilde{b}'_\theta = 0 \quad (10)$$

Given that BM19 did not show the detailed derivation process of equation (10), while this work will carefully present this process to reproduce the equation (10) (see Appendix A), the purpose of which is to figure out how to obtain this equation (10) in detail, especially, clarifying the mathematical and physical conditions that the equation (10) is required to satisfy.

Introducing a variable $y(x)$ as follows

$$y(x) = \sqrt{(1-x^2)(1+\beta^2x^2)}\tilde{b}'_\theta(x) \quad (11)$$

Taking the formula (11) into the formula (10), focusing on the low-latitude region and removing the higher-order term (i.e., $O(x^4)$, see the formula (B8) in Appendix B), we can derive the following equation (12), which is just the equation (46) in BM19.

$$\frac{\partial^2y}{\partial x^2} - (\alpha_0x^2 - \alpha_1)y = 0 \quad (12)$$

where, $\alpha_0 = -\frac{C^2}{M(0)} - \frac{mC}{M(0)}(1-\beta^2) + 2(m^2-1) - 2\beta^2(\beta^2+1)$;

$\alpha_1 = \frac{mC}{M(0)} - m^2 + 1 - \beta^2$.

In physics, the equation (12) is called as the 'Weber equation', the derivation of which involves the so-called truncation treatment, i.e., discarding the higher-order term (i.e., $O(x^4)$), which depends on the latitude. Here, the question is that whether removing the $O(x^4)$ term can induce the significant truncation errors for the results? This work further makes the perturbation analysis (see Appendix C) to check the accuracy of the results, which shows that the 'Weber equation' is valid to study the low-latitude waves. For example, when the latitude is smaller than 25 degrees, the relative errors caused by the truncation treatment is shown to be less than 5%.

2.3. Specific solution of the 'Weber equation'

Here, we will further focus on the specific solution of the equation (12). Defining $\xi = \tilde{\alpha}x$ (here, $\tilde{\alpha} = \alpha_0^{\frac{1}{4}}$), the equation (12) can be further transformed into

$$\frac{\partial^2 y}{\partial \xi^2} + (\tilde{\eta} - \xi^2)y = 0 \tag{13}$$

where, $\tilde{\eta} = \alpha_0^{-\frac{1}{2}}\alpha_1$, the relative errors of $\tilde{\eta}$ (caused by the truncation treatment) are discussed in Appendix C.

After this transformation, the form of equation (13) is completely same as the energy eigen-equation of one-dimensional harmonic oscillator in quantum mechanics. Actually, the specific solution to the equation that has the same mathematical form as the equation (13) has been discussed in quantum mechanics. Here, we would like to briefly recall it. Assuming the specific solution to the equation (13) has the following form

$$y(\xi) = AH(\xi)e^{-\frac{\xi^2}{2}} \tag{14}$$

where, A is a constant coefficient unrelated to ξ.

Taking $y(\xi)$ into the equation (13), we can obtain a second-order differential equation as follows

$$H''(\xi) - 2\xi H'(\xi) + (\tilde{\eta} - 1)H(\xi) = 0 \tag{15}$$

When $\tilde{\eta}$ satisfies the expression (namely $\tilde{\eta} - 1 = 2n$, here, n=0,1,2⋯), we can show the

specific polynomial solution (i.e., $H_n(\xi)$)to the equation (15), i.e., $H_n(\xi) = (-1)^n e^{\xi^2} \frac{d^n}{d\xi^n}(e^{-\xi^2})$, which is called as the Hermite polynomial of degree *n* and satisfies the following Hermite differential equation

$$H_n''(\xi) - 2\xi H_n'(\xi) + 2nH_n(\xi) = 0 \tag{16}$$

Furthermore, we can give the specific solution (i.e., $y_n(\xi)$) of the equation (13) as follows

$$y_n(\xi) = A_n e^{-\frac{1}{2}\xi^2} H_n(\xi) \tag{17}$$

where, $A_n = \sqrt{\frac{\tilde{\alpha}}{\sqrt{\pi}2^n n!}}$, being a normalized coefficient.

Note that the above expression (i.e., $\tilde{\eta}(= \alpha_0^{-\frac{1}{2}}\alpha_1) = 2n + 1$) is equivalent to $\alpha_1 = (2n + 1)\sqrt{\alpha_0}$, here, both α_0 and α_1 are complex numbers and they are related to $\chi(= 1 + \frac{i\eta k^2}{\tilde{\omega}})$, where the magnetic diffusivity $\eta(= \frac{1}{\mu\sigma})$ can induce the ohmic dissipation (i.e., damping effects) of the waves, the details of which will be shown in section 3.1.

Moreover, we can rigorously prove that the expression (i.e., $\tilde{\eta} = 2n + 1$ alternatively $\alpha_1 = (2n + 1)\sqrt{\alpha_0}$) is the sufficient and necessary condition that the equation (15) owns the Hermite polynomial solution, i.e., $H_n(\xi)$ (Proof is shown in Appendix D). Nevertheless, here a question may arise: Whether the specific solution (i.e., $y_n(\xi)$) and the expression (i.e., $\alpha_1 = (2n + 1)\sqrt{\alpha_0}$) can be valid in the actual geophysical situation? As mentioned above, Knezek and Buffett (2019) found that the Hermite basis functions indexed by *n* (see their formula (1), which owns the same form as that of the above formula (17)) can be chose to fit the observed equatorial waves, while the above discussion may just provide the theory basis to show the existence of the Hermite polynomial of degree *n* for representing the equatorial waves. Therefore, the previous work (Knezek and Buffett, 2019) actually provides the observed evidence to show that the specific solution $y_n(\xi)$ (or $H_n(\xi)$) can exist in the reality, which means that, in the actual situation, the condition (i.e., $\alpha_1 = (2n + 1)\sqrt{\alpha_0}$) also can be valid (see the 'Proof of the sufficiency' in Appendix D).

Here, we further show the specific solution to the 'Weber equation' as follows (Proof is shown in Appendix E)

$$y_n(x) = A_n e^{-\frac{1}{2}\tilde{\alpha}^2 x^2} H_n(\tilde{\alpha}x) \tag{18}$$

where, $\tilde{\alpha} = \alpha_0^{\frac{1}{4}}$; $\alpha_0^{-\frac{1}{2}}\alpha_1 = 2n+1$, n=0,1,2,⋯.

In summary, the amplitude of the perturbed magnetic field (i.e., $\tilde{b}'_\theta(x)$) changes with latitude (except the north and south poles due to the singularities) satisfies the equation (10), which is shown to be valid on the subdecadal (e.g., the 8.5yr period) scales, where the inertia term I is shown to be much weaker than the magnetic force term M (see the discussion part); when the region is confined to near the equator, the equation (10) will be further transformed into the equation (12). The perturbation analysis (see Appendix C) further shows that the related results (i.e., $y_n(x)$, $\tilde{\alpha}$, $\tilde{\eta}$) derived from the equation (12) are reliable to analyze the low-latitude waves, e.g., when the latitude is below 25°, the relative errors are shown to be less than 5%, and these errors will be further reduced as the latitude decreases. Hence, discussion of the equation (12) and its specific solutions (i.e., formula (18)) is significant to deeply understand the origins of the observed low-latitude waves on the subdecadal scales. Despite this, the first thing required here is to determine whether the formula (18) owns the equatorial confinement property.

2.4. Simulation of the low-latitude distribution features

Formula (18) can represent the low-latitude distribution features of the MAC waves of degree n. Here, we will further show this point. For the sake of simplicity, we only present the Hermite functions with the several lower degrees (i.e., n=0, 1, 2 and 3): $H_0(x) = 1$, $H_1(x) = 2x$, $H_2(x) = 4x^2 - 2$, $H_3(x) = 4x(2x^2 - 3)$. Thus, the expressions of $y_n(x)$ are listed as following

when n=0, $y_0(x) = \tilde{\alpha}^{\frac{1}{2}}\pi^{-\frac{1}{4}}e^{-\frac{1}{2}\tilde{\alpha}^2x^2}$;

when n=1, $y_1(x) = \sqrt{2}\tilde{\alpha}^{\frac{3}{2}}\pi^{-\frac{1}{4}}xe^{-\frac{1}{2}\tilde{\alpha}^2x^2}$;

when n=2, $y_2(x) = 2^{-\frac{1}{2}}\tilde{\alpha}^{\frac{1}{2}}\pi^{-\frac{1}{4}}(2\tilde{\alpha}^2x^2 - 1)e^{-\frac{1}{2}\tilde{\alpha}^2x^2}$;

when n=3, $y_3(x) = 3^{-\frac{1}{2}}\pi^{-\frac{1}{4}}\tilde{\alpha}^{\frac{3}{2}}x(2\tilde{\alpha}^2x^2 - 3)e^{-\frac{1}{2}\tilde{\alpha}^2x^2}$.

From these expressions, $y_n(x)$ depends on the parameter $\tilde{\alpha}$ (i.e., $\tilde{\alpha} = \alpha_0^{\frac{1}{4}}$), where, α_0 is expressed by $\alpha_0 = -\frac{C^2}{M(0)} - \frac{mC}{M(0)}(1-\beta^2) + 2(m^2-1) - 2\beta^2(\beta^2+1)$. Although $\tilde{\alpha}$ is a complex number, here we synthetically set various $\tilde{\alpha}$ values as the real numbers to show the potential properties of $y_n(x)$. In the section 3.3, we will further use the relevantly physical

parameters (see Table 1) to estimate the real (or close to be real) $\tilde{\alpha}$ value.

Here, the synthetical results are displayed in Figure 1, showing that $\tilde{\alpha}$ can influence the equatorial confinement degree. In general, if $\tilde{\alpha}$ is small (e.g., $\tilde{\alpha} \leq 1$), then $y_n(x)$ curves cannot perform the low-latitude concentration behaviors; if $\tilde{\alpha}$ is larger, then $y_n(x)$ curves can be more concentrated to the equatorial areas, especially, when $\tilde{\alpha} \geq \sim 4$, the $y_n(x)$ curves are shown to be obviously assembled and confined to the low-latitude regions (within ~ ±30°). Consequently, the appearance of eMAC waves requires a relatively larger $\tilde{\alpha}$ value. Additionally, Figure 1 shows that, when n is an even number (e.g., n=0,2,⋯), $y_n(x)$ is an even function with respect to x (see Figure 1 (a) and (c)); when n is an odd number (e.g., n=1,3,⋯), $y_n(x)$ will be an odd function (see Figure 1 (b) and (d)), meaning that the eMAC waves can present the symmetric or antisymmetric features with respect to the equator.

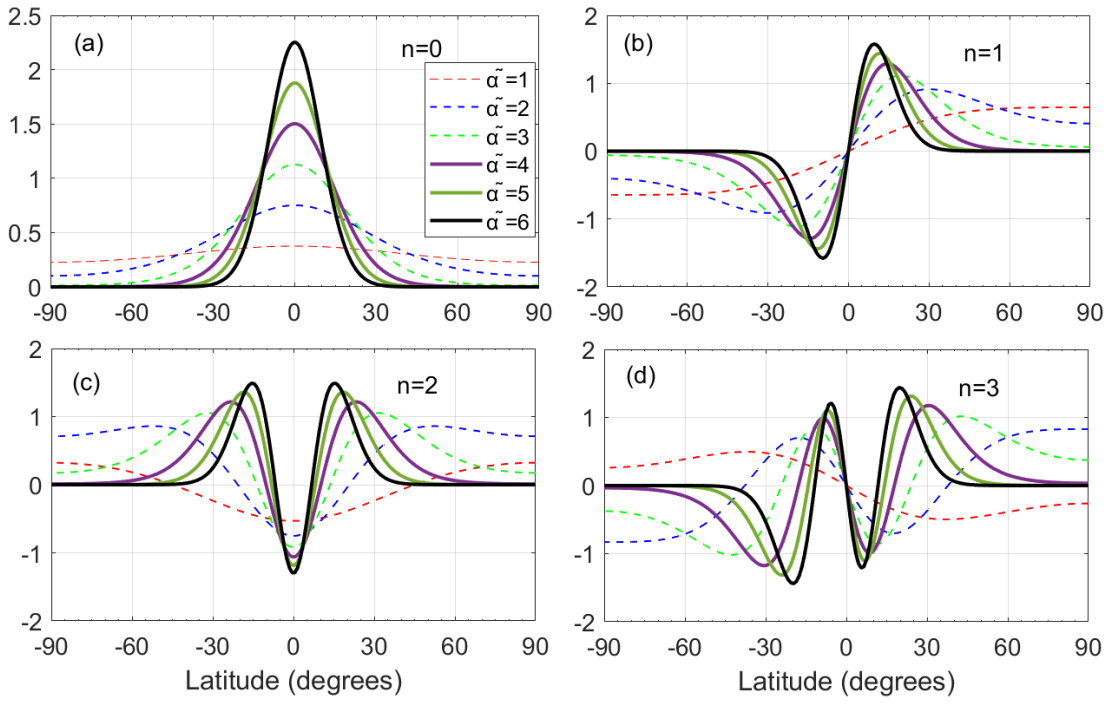

Figure 1. Numerical simulation of the low-latitude distribution of the MAC waves by means of synthetic setting various $\tilde{\alpha}$ values (here, $\tilde{\alpha}$ is set to be the real numbers). When $\tilde{\alpha}$ value is large enough (i.e., $\tilde{\alpha} \geq \sim 4$), the amplitudes of these waves can perform the obviously equatorially trapped behaviors, i.e., the wave energy can be strongly confined to the low-latitude region (within ~ ± 30°).

3.Results

3.1. On the damping rate and eigen-period formulas

As mentioned above, this work presents the specific solution (i.e., formula (18)) to the

equation (12), and we have

$$\alpha_1 = (2n+1)\sqrt{\alpha_0} \tag{19}$$

where, $\alpha_0 = -\frac{4\Omega^2 R^2 \chi}{V_a^2(0)N^2}\tilde{\omega}^2 - \frac{2\Omega m\chi}{V_a^2(0)k^2}(1-\beta^2)\tilde{\omega} + 2(m^2-1) - 2\beta^2(\beta^2+1)$;

$\alpha_1 = \frac{2\Omega m\chi}{V_a^2(0)k^2}\tilde{\omega} + 1 - m^2 - \beta^2$.

Here, we can further write the following formula

$$D_n\tilde{\omega}^2 + E_n\tilde{\omega} + F_n = 0 \tag{20}$$

where, $D_n = \frac{m^2\chi^2}{V_a^2(0)k^4} + (2n+1)^2\frac{R^2\chi}{N^2}$; $E_n = \frac{m\chi}{2\Omega k^2}[2(1-m^2-\beta^2) + (2n+1)^2(1-\beta^2)]$;

$F_n = \frac{V_a^2(0)}{4\Omega^2}[(1-m^2-\beta^2)^2 - 2(2n+1)^2(m^2-1-\beta^4-\beta^2)]$.

Formula (20) expresses a complex equation, both the imaginary and real parts of which are required to be 0, from which the formulas of damping rate α and eigen-frequency ω of the eMAC waves can be derived.

Firstly, the imaginary part of equation (20) is equal to 0, we have

$$A_n\alpha = -\eta k^2 B_n \tag{21}$$

where, $A_n = [\frac{2m^2}{V_a^2(0)k^4} + 2(2n+1)^2\frac{R^2}{N^2}]\omega + \frac{m}{2\Omega k^2}[2(1-m^2-\beta^2) + (2n+1)^2(1-\beta^2)]$;

$B_n = [\frac{2m^2}{V_a^2(0)k^4} + (2n+1)^2\frac{R^2}{N^2}]\omega + \frac{m}{2\Omega k^2}[2(1-m^2-\beta^2) + (2n+1)^2(1-\beta^2)]$;

Here, the damping rate α is expressed by

$$\alpha = -\eta k^2\gamma \tag{22}$$

where, $\gamma = \frac{B_n}{A_n}$, $\gamma \neq 1$.

Formula (22) shows that the damping rate α is proportional to the magnetic diffusivity $\eta(=\frac{1}{\mu\sigma})$, meaning that the electrical conductivity σ atop the Earth's core plays an important role in causing the ohmic dissipation of the waves. In order to well understand α, we need to study the γ value, which superficially depends on the space wave number *m*, the Alfvén wave velocity $V_a(0)$ at the equator and the stratification (*N*, *H*). When *N* is in the range of 7~15Ω (see Table 1) and $\omega = \frac{2\pi}{T}$ (here, *T* being 8.5yr), the γ values are shown in Figure 2. Since A_n can be equal to 0, so the discontinuous points (DPs) or the singularities (i.e., *n*=0, *H*~18.8km; *n*=1, *H*~19km; *n*=2, *H*~20km; *n*=3, *H* is shown to be in the range of 20~25km) can appear in Figure 2.

Besides, Figure 2 also shows that when H values (for each degree mode) are on the right side of the DPs, γ values are shown to be close to be 1. It should be noted that, here we will mainly concern the γ values at the right side of DPs, since the estimated H values (reflected by the red vertical dashed lines in the local enlarged drawings) inferred from the eigen-periods of eMAC waves matching the 8.5yr (see the following text) are shown to mainly locate at this side.

The exact changes of γ values (with N and H) are further shown in the local enlarged drawings (see Figure 2), which shows that γ values can quickly tend toward 1 with H increase, especially, the greater the buoyancy frequency N is, the faster the γ values approach to 1 (note that $\gamma \neq 1$). When $\gamma \to 1$, the α formula will be simplified as $\alpha \to -\eta k^2 = -\frac{j^2\pi^2}{\mu\sigma H^2}$, which means that the damping effects of the eMAC waves mainly depend on σ and H^2, while the corresponding relaxation time τ is written as $\tau = \frac{1}{|\alpha|} \to \frac{\mu\sigma H^2}{j^2\pi^2}$. Of course, the damping rate α is also related to the vertical wave number j, but, if j >1 (e.g., 2,3,⋯), the damping dissipation effects will be too strong to effectively produce these travelling waves. Therefore, we mainly consider the case of j =1 and express the damping rate as a simple formula, i.e., $\alpha \approx -\eta k^2 = -\frac{\pi^2}{\mu\sigma H^2}$.

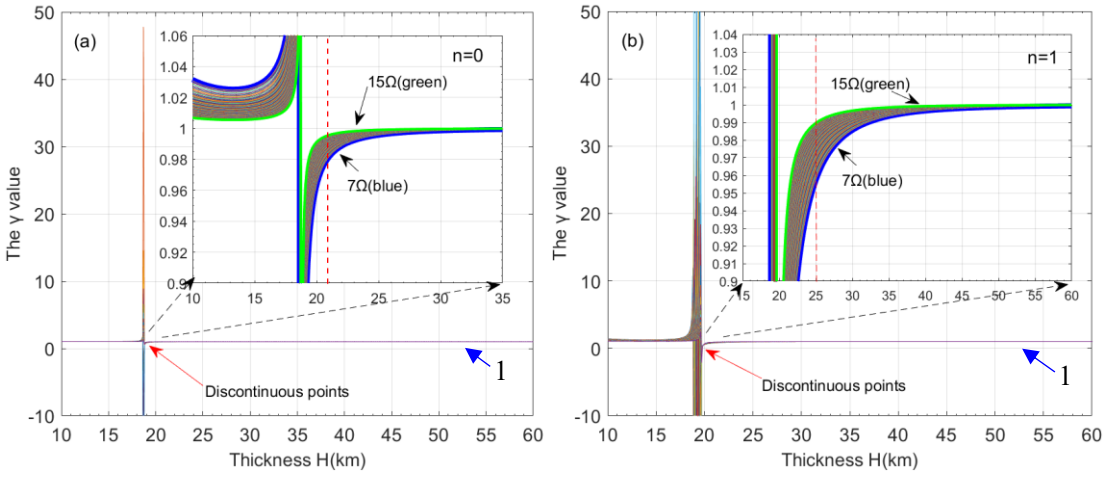

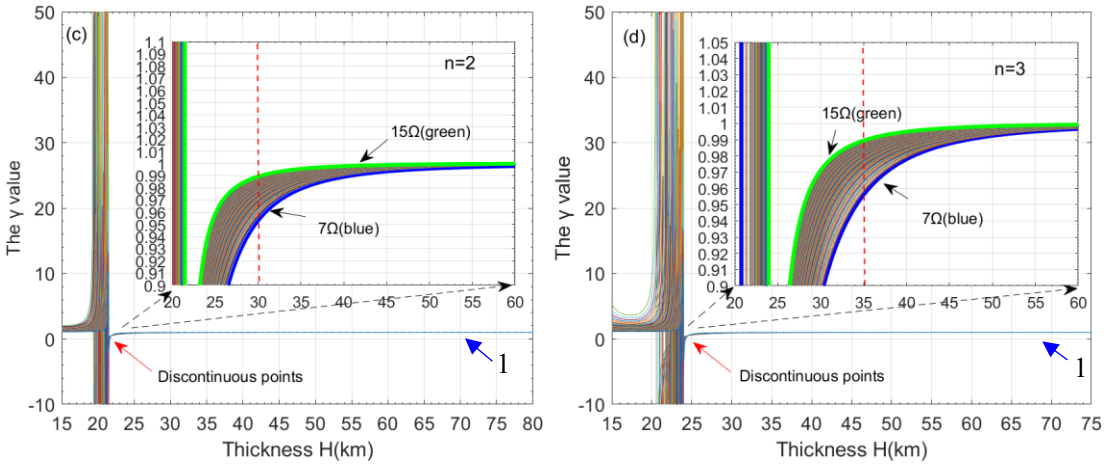

Figure 2. The γ values change with the stratification parameters (i.e., *H* and *N*). Here, *N* is in the range of 7~15Ω. The green curves (upper border) being the case of *N*=15Ω, while the blue curves (lower border) being the case of *N*=7Ω. The red vertical dashed lines (shown in the enlarged drawings) show the corresponding *H* values, which are estimated by the eMAC waves with the 8.5yr eigen-period (see the following text).

Secondly, the real part of equation (20) is equal to 0, we obtain

$$\tilde{D}_n\omega^2 + \tilde{E}_n\omega + \tilde{F}_n = 0 \tag{23}$$

where, $\tilde{D}_n = \frac{m^2}{V_a^2(0)k^4} + (2n+1)^2\frac{R^2}{N^2} = \frac{\rho_0\mu m^2H^4}{B_r^2(0)\pi^4} + (2n+1)^2\frac{R^2}{N^2}$;

$\tilde{E}_n = \frac{m}{2\Omega k^2}[2(1-m^2-\beta^2) + (2n+1)^2(1-\beta^2)] = \frac{mH^2}{2\Omega\pi^2}[2(1-m^2-\beta^2) + (2n+1)^2(1-\beta^2)]$;

$\tilde{F}_n = F_n - \frac{m^2}{V_a^2(0)k^4}(\alpha+\eta k^2)^2 - (2n+1)^2\frac{R^2}{N^2}(\alpha^2+\alpha\eta k^2)$.

Using $\alpha = -\eta k^2\gamma$ (the formula (22)), $\tilde{F}_n$ can be further expressed by

$$\tilde{F}_n = F_n - \underbrace{\frac{m^2}{V_a^2(0)}\eta^2(1-\gamma)^2}_{T_1} - \underbrace{(2n+1)^2\frac{R^2}{N^2}(\eta k^2)^2\gamma(\gamma-1)}_{T_2} \tag{24}$$

where, $F_n = \frac{V_a^2(0)}{4\Omega^2}[(1-m^2-\beta^2)^2 - 2(2n+1)^2(m^2-1-\beta^4-\beta^2)]$.

Since γ $(=\frac{B_n}{A_n})$ includes ω (see the formulas (21) and (22)), so $\tilde{F}_n$ also includes ω, which means that the equation (23) does not express a quadratic equation with respect to ω. However, using $\gamma \to 1$, both T_1 and T_2 terms in formula (24) are shown to be much smaller than F_n. Hence, both T_1 and T_2 terms are removed from $\tilde{F}_n$, thus

$$\tilde{F}_n \to F_n$$

so, formula (23) is further turned into the following typical quadratic equation regarding ω

$$\widetilde{D}_n\omega^2 + \tilde{E}_n\omega + F_n = 0 \tag{25}$$

Solving the equation (25), we have

$$\omega = \frac{-\tilde{E}_n \pm \sqrt{\tilde{E}_n{}^2 - 4\,\widetilde{D}_n F_n}}{2\,\widetilde{D}_n} \tag{26}$$

Because the term (i.e., $4\,\widetilde{D}_n F_n$) is comparable with $\tilde{E}_n{}^2$ (e.g., for n=0, H=20km, N=7Ω, $\frac{4\,\widetilde{D}_n F_n}{\tilde{E}_n{}^2}$~0.95; for n=1, $\frac{4\,\widetilde{D}_n F_n}{\tilde{E}_n{}^2}$~0.61), the equation (25) presents two different real roots, which are respectively expressed by $\omega_{n,1}$ and $\omega_{n,2}$ (the eigen-periods are respectively expressed as $T_{n,1} = \frac{2\pi}{\omega_{n,1}}$ and $T_{n,2} = \frac{2\pi}{\omega_{n,2}}$)

$$\left.\begin{aligned} \omega_{n,1} &= \frac{-\tilde{E}_n + \sqrt{\tilde{E}_n{}^2 - 4\,\widetilde{D}_n F_n}}{2\,\widetilde{D}_n} \\ \omega_{n,2} &= \frac{-\tilde{E}_n - \sqrt{\tilde{E}_n{}^2 - 4\,\widetilde{D}_n F_n}}{2\,\widetilde{D}_n} \end{aligned}\right\} \tag{27}$$

where, $0 < \omega_{n,2} < \omega_{n,1}$.

From the above formulas, these physical factors (i.e., m, β, ρ_0, $B_r(0)$, N, H) can influence the eigen-periods of the eMAC waves. Nevertheless, the following several parameters (i.e., m, β, ρ_0, $B_r(0)$) are considered as the known factors (see Table 1), so the eigen-periods will mainly depend on the stratification parameters (i.e., N and H). Figure 3 shows that the results of the eigen-periods change with N and H. Although the modes (e.g., n=0 and n=1) may present two eigen-period curves (i.e., $T_{n,1}$ and $T_{n,2}$ in Figure 3), only one root (i.e., $T_{n,1}$) can be valid to match the 8.5yr period, and the target solutions are further displayed by the blue boxes in Figure 3, where the coordinates (H, T) of these boxes represent the thickness-period values. For example, the blue box 1 in Figure 3(a) represents H~21km, which is estimated by the eigen-period $T_{0,1}$(=8.5yr); Figure 3(b) shows the mode n=1, when $T_{1,1}$ matches the 8.5yr, H is estimated to be 25km (i.e., the box 2); Figure 3(c) and (d) respectively display the modes n=2 and 3, where, boxes 3 and 4 show that the estimated H values are 30km and 35km respectively, when the eigen-periods match the 8.5yr period. Besides, the eigen-period curves own the good convergent property, meaning that the eigen-periods are unrelated to N, which is due to the large enough N values (i.e., 7Ω~15Ω) used in this work. As BM19 suggested, if N is larger than a threshold value, the eigen-period will not be influenced by N. Here we can verify that this threshold value should be smaller than 7Ω.

It is worth highlighting that, all the H values (i.e., for n=0, H=21km; for n=1, H=25km; for

n=2, H=30km; for n=3, H=35km) estimated by the 8.5yr period can make the corresponding γ values be close to 1: For example, for n=0, γ will be 0.98~0.99, while for n=1,2,3, γ value will be 0.95~0.99, which can be inferred from the Figure 2 (see the red vertical dashed lines in the enlarged drawings). Consequently, we confirm that the above expression (i.e., $\tilde{F}_n \to F_n$) is valid and the formula (25) is reliable as well.

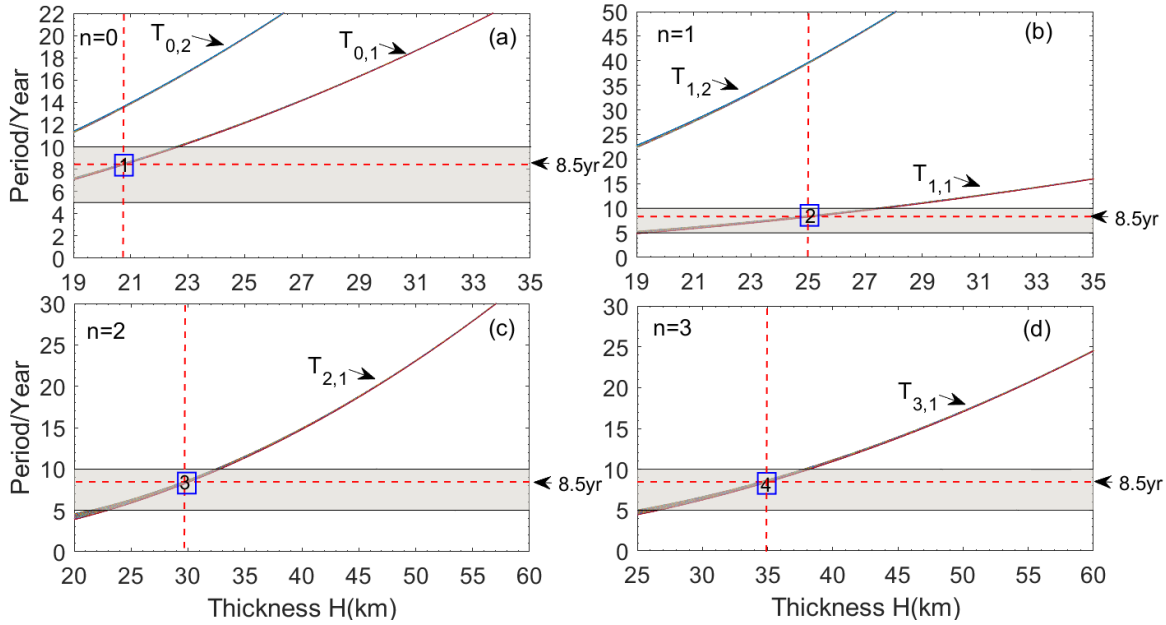

Figure 3. Eigen-periods of the eMAC waves vary with N and H, where N is set to be 7~15Ω, H>19km (for n=0,1), H>20km (for n=2), H>25km (for n=3); the gray shadow regions show the subdecadal periods (i.e., 5~10yr scales); the red horizontal dashed lines show the 8.5yr period; the coordinates of the blue boxes show the corresponding thickness-period (H, T) values, i.e., box 1 (21km, 8.5yr), box 2 (25km, 8.5yr), box 3(30km, 8.5yr), box 4 (35km, 8.5yr).

Combining the α and ω formulas, we give the expression of quality factor Q

$$Q = \frac{Re(\tilde{\omega})}{2\,Im(\tilde{\omega})} = \frac{\omega}{2|\alpha|} = \frac{\pi}{\eta\gamma k^2 T} = \frac{\mu\sigma H^2}{\pi\gamma T} \tag{28}$$

where, T refers to the eigen-period of the eMAC wave modes.

Using T=8.5, we present the estimated Q values in Table 2 (here, we adopt γ =1), which are shown to be quite small, i.e., only 1~2. Because of these small Q values, the excitations of eMAC waves should be durative, otherwise, these excited waves will rapidly disappear due to the strongly ohmic dissipation. However, the exact excitation mechanism responsible for the continual generation of these eMAC waves is still unclear (e.g., Gillet et al, 2021), though the convection

within the Earth's core may provide a mainly stochastic excitation source (e.g., Buffett and Knezek, 2018; Gillet et al, 2021). Additionally, BM19 referred to an alternatively physical mechanism responsible for these excitations, that is, the westward drift of buoyance plumes in the equatorial areas, which may generate the eMAC waves through either the influence of fluid rising into the stratification layer atop of Earth's core or magnetic disturbances at the bottom of this stratified layer.

Table 2 Related parameters of eMAC waves with different degrees (here, T=8.5yr)

degree n	H (km)	Q	τ (yr)	L (km)
0	21.0	0.66	1.78	658.6
1	25.0	0.93	2.52	932.4
2	30.0	1.34	3.63	1343.1
3	35.0	1.83	4.95	1831.5

3.2. Propagation speeds of the eMAC waves

Based on the above discussion, the theoretical propagation velocity (i.e., phase speed) of the eMAC waves with the 8.5yr period is given by

$$V = \frac{\omega}{m} = \frac{-\tilde{E}_n + \sqrt{\tilde{E}_n{}^2 - 4\,\tilde{D}_n F_n}}{2m\,\tilde{D}_n} \tag{29}$$

where, the sign of V (or ω) reflects the propagation direction of the eMAC waves, $V > 0$ refers to the eastward propagation, while $V < 0$ means propagating westward, which is helpful to identify whether the observed equatorial waves (e.g., Chulliat et al, 2015; Chi-Durán et al, 2020) are eMAC waves.

Here, we show that $\tilde{E}_n = \frac{mH^2}{2\Omega\pi^2}[2(1-m^2-\beta^2)+(2n+1)^2(1-\beta^2)]<0$ (based on the parameters shown in Table 1) and $\tilde{D}_n = \frac{\rho_0\mu m^2 H^4}{B_r^2(0)\pi^4} + (2n+1)^2\frac{R^2}{N^2}>0$, so $V > 0$, meaning that the propagation direction of the eMAC waves with the 8.5yr period is predicted to be eastward. Moreover, the theoretical linear velocity of the eMAC waves can be calculated by $V^L = RV$. Defining $V^L = \frac{-\tilde{E}_n + \sqrt{\tilde{E}_n{}^2 - 4\,\tilde{D}_n F_n}}{2m\,\tilde{D}_n} R$, the results are displayed in Figure 4, which shows that the V^L can match the observed result (i.e., 345~477 km/yr reflected by the shallow area in Figure 4), where, the predicted velocity is ~370km/yr, which is shown by the red dashed lines. Additionally,

the propagating distances (L) of these waves within the relaxation time (τ) are also estimated, see Table 2.

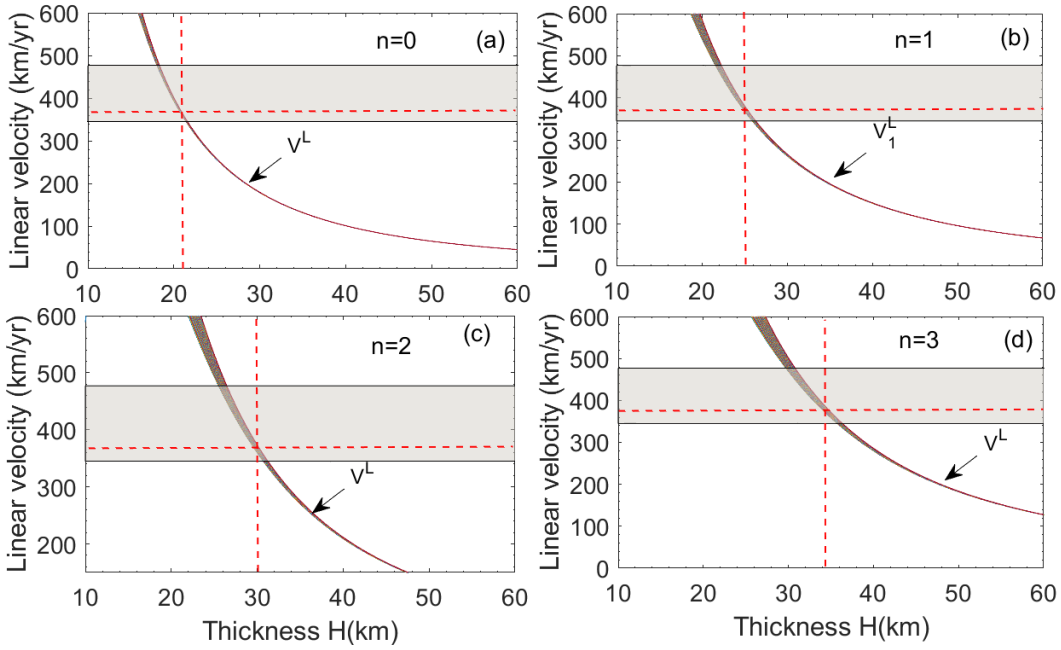

Figure 4. Predicted linear velocities of eMAC waves vary with H and N (here m=7); the blue shallow area shows the rang of the observed liner velocity (i.e., 345~477km/yr) cited from Chi-Durán et al (2020).

3.3. On the equatorial confinement property of the MAC waves

By synthetically varying the $\tilde{\alpha}$ values, Figure 1 presents the potential latitudinal distribution characteristics of the MAC waves. Here, further using the related parameters (see Table 1), which are considered to be (or close to be) the actual Earth situation, we will estimate the $\tilde{\alpha}$ values to determine whether the MAC waves own the equatorial confinement property. Since α_0 is a complex quantity, while $\tilde{\alpha}$ is determined by α_0 (i.e., $\tilde{\alpha} = \alpha_0^{\frac{1}{4}}$), so $\tilde{\alpha}$ is also a complex quantity. Here, we write

$$\alpha_0 = Re(\alpha_0) + iIm(\alpha_0) \text{ and } \tilde{\alpha} = Re(\tilde{\alpha}) + iIm(\tilde{\alpha})$$

Moreover, $Re(\alpha_0)$ and $Im(\alpha_0)$ are written as

$$\left.\begin{aligned} Re(\alpha_0) &= -\frac{4\Omega^2R^2}{V_a^2(0)N^2}[\omega^2 - \alpha(\alpha+\eta k^2)] - \frac{2\Omega m}{V_a^2(0)k^2}(1-\beta^2)\omega + 2(m^2-1) - 2\beta^2(\beta^2+1) \\ Im(\alpha_0) &= -\frac{4\Omega^2R^2}{V_a^2(0)N^2}\omega(2\alpha+\eta k^2) - \frac{2\Omega m}{V_a^2(0)k^2}(1-\beta^2)(\alpha+\eta k^2) \end{aligned}\right\} \quad (30)$$

where, $k = \frac{\pi}{H}$, $V_a(0) = \frac{B_r(0)}{\sqrt{\rho_0\mu}}$.

Using $\alpha \approx -\eta k^2 = -\eta\frac{\pi^2}{H^2}$, we present the following equation

$$\left.\begin{aligned} Re(\alpha_0) &\approx -\underbrace{\frac{4\Omega^2R^2\mu\rho_0}{B_r^2(0)N^2}\omega^2}_{1} - \underbrace{\frac{2\Omega m\mu\rho_0H^2}{B_r^2(0)\pi^2}(1-\beta^2)\omega}_{2} + \underbrace{2(m^2-1)}_{3} - \underbrace{2\beta^2(\beta^2+1)}_{4} \\ Im(\alpha_0) &\approx \frac{4\mu\rho_0\Omega^2R^2\pi^2}{B_r^2(0)N^2H^2}\omega\eta \end{aligned}\right\} \quad (31)$$

Formula (31) shows that these physical factors (i.e., ρ_0, m, β, $B_r(0)$, N and H) jointly influence the α_0 value, and then affect the low-latitude confinement degree of the waves. Taking the related parameters (Table 1) into the formula (31), we can estimate the values of $Re(\alpha_0)$, $Im(\alpha_0)$, $Re(\tilde{\alpha})$ and $Im(\tilde{\alpha})$, see Table 3. The results indicate that $Im(\tilde{\alpha}) \ll Re(\tilde{\alpha})$, here, $Re(\tilde{\alpha})$ values are estimated to be in an approximate range (i.e., 3.5~4.3), which are large enough (see Figure 1) to enable the equatorial confinement of the waves, see Figure 5(a), (b), (c) and (d), where the real parts of $y_n(x)$ (i.e., $Re[y_n(x)]$; n=0,1,2,3; β =1.58) are displayed and they are shown to be insensitive to the N values ($7\Omega \le N \le 15\Omega$). Besides, we also consider the case of $\beta = 0$ (see Figure 5(e) and (f)), which shows that the $y_n(x)$ curves do not present the equatorial confinement property, meaning that the eMAC waves cannot appear in the case of the CMB radial magnetic fields being constant with respect to the latitude. The above results imply that the gradient strength of the radial magnetic field over the CMB surface (characterized by the parameter β) may provide the so-called wave guide to produce the low-latitude confinement property for the MAC waves.

Here, we also note that $y_n(x)$ (estimated by the related parameters listed in Table 1) cannot rapidly decay to 0 at the regions with the latitude > 30° (especially for the relatively higher degree modes, e.g., n=3), though $y_n(x)$ results can generally present the equatorial confinement features (Figure 5(a), (b), (c) and (d)). Note that the relatively larger errors for $y_n(x)$ itself may exist in the higher latitude regions, hence $y_n(x)$ possibly might not well reflect the real situation locating at the higher latitude. Hence, it is necessary to make clear all the potential physical factors that can increase the equatorial confinement degree of the MAC wave model, the detailed information of which is shown in the discussion part. Nevertheless, the $y_n(x)$ results are shown to be reliable to characterize the property of the waves locating at the low-latitude regions, for example, if the latitude is below 25 degrees, then the relative errors of $y_n(x)$ are shown to be smaller than 5% (see the Appendix C).

Table 3 The values of parameters (α_0 and $\tilde{\alpha}$) estimated by the different degree modes with the same

552 eigen-period ($T = \frac{2\pi}{\omega}$ =8.5yr). Here, N=10Ω suggested by Knezek and Buffett (2018).

n	H (km)	$Re(\alpha_0)$	$Im(\alpha_0)$	$Re(\tilde{\alpha})$	$Im(\tilde{\alpha})$
0	21.0	158.49	12.13	3.55	0.068
1	25.0	198.53	8.56	3.75	0.040
2	30.0	258.36	5.94	4.01	0.023
3	35.0	329.09	4.37	4.26	0.014

553

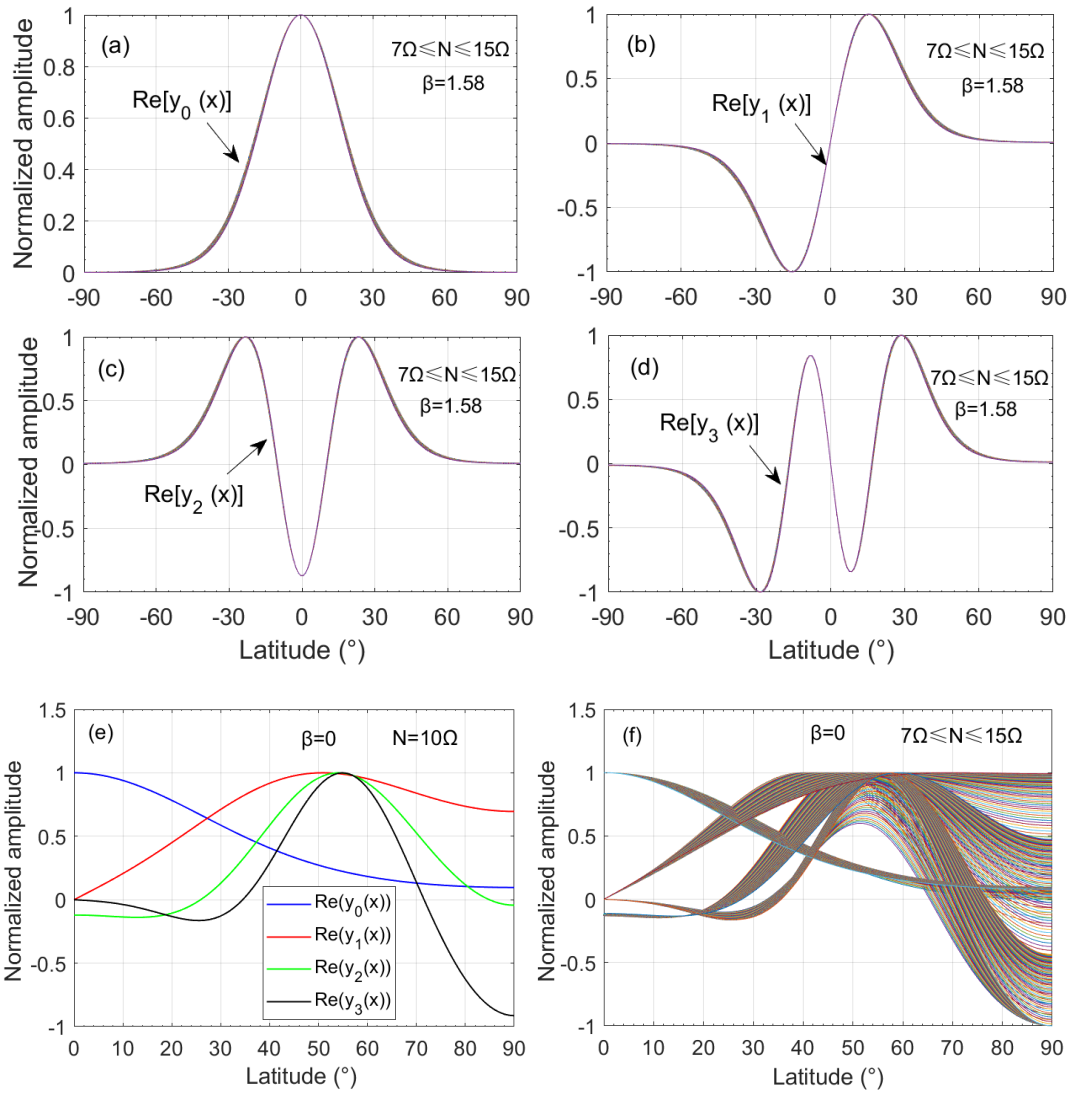

554

555

556 **Figure 5**. Equatorially trapped characteristics of MAC waves with the degrees (n=0,1,2,3). In this figure, Re (.)

557 refers to taking the real part of $y_n(x) = A_n e^{-\frac{1}{2}\tilde{\alpha}^2 x^2} H_n(\tilde{\alpha}x)$. (a), (b), (c) and (d) present the results of $y_n(x)$

558 (n=0,1,2,3 respectively) in the case of β=1.58, while (e) and (f) show the results in the case of β=0.

559

560 **3.4. On the perturbed magnetic field model due to eMAC waves**

According to the formula (6) and the relationship ($b'_\theta = \sqrt{1-x^2}b_\theta$ and $b'_\varphi = \frac{1}{\sqrt{1-x^2}}b_\varphi$), we can give the perturbed magnetic field models (i.e., b_θ and b_φ) as follows

$$\begin{cases} b_\theta = \frac{1}{\sqrt{1-x^2}}\tilde{b}'_\theta(x)\, sin(\, kz)\, exp[\, i(m\varphi - \tilde{\omega}\tilde{t})] \\ b_\varphi = \sqrt{1-x^2}\tilde{b}'_\varphi(x)\, sin(\, kz)\, exp[\, i(m\varphi - \tilde{\omega}\tilde{t})] \end{cases} \tag{32}$$

where, $z = r - R$; $\tilde{t} = t - t_0$, t_0 refers to the initial time.

Defining

$$\tilde{b}_{\theta_n}(x) = \frac{1}{\sqrt{1-x^2}}\tilde{b}'_{\theta_n}(x) \text{ and } \tilde{b}_{\varphi_n}(x) = \sqrt{1-x^2}\tilde{b}'_{\varphi_n}(x) \tag{33}$$

So, the perturbed magnetic field models (of the degree n) are expressed by

$$\left.\begin{aligned} b_{\theta_n} &= \tilde{b}_{\theta_n}(x)\, sin(\, kz)\, exp(\, im\varphi - \tilde{\omega}t) \\ b_{\varphi_n} &= \tilde{b}_{\varphi_n}(x)\, sin(\, kz)\, exp(\, im\varphi - \tilde{\omega}t) \end{aligned}\right\} \tag{34}$$

where, $\tilde{b}_{\theta_n}(x)$ and $\tilde{b}_{\varphi_n}(x)$ respectively reflect the amplitudes and the latitudinal distribution features of b_{θ_n} and b_{φ_n}.

According to the formula (11), we have $\tilde{b}'_\theta(x) = \frac{1}{\sqrt{(1-x^2)(1+\beta^2x^2)}}y(x)$. Here, we further write

$$\tilde{b}'_{\theta_n}(x) = \frac{1}{\sqrt{(1-x^2)(1+\beta^2x^2)}}y_n(x) \tag{35}$$

Therefore

$$\tilde{b}_{\theta_n}(x) = \frac{1}{\sqrt{1-x^2}}\tilde{b}'_{\theta_n}(x) = \frac{1}{(1-x^2)\sqrt{1+\beta^2x^2}}y_n(x) \tag{36}$$

Focusing on the low-latitude regions and adopting the series expansion approach, that is, $\frac{1}{1-x^2} = 1 + x^2 + \underbrace{x^4 + x^6 + \cdots}_{O(x^4)}$, then, removing the higher-order quantity (i.e., $O(x^4)$), we obtain

$$\tilde{b}_{\theta_n}(x) = \frac{1+x^2}{\sqrt{1+\beta^2x^2}}y_n(x) \tag{37}$$

where, the truncation errors caused by removing $O(x^4)$ are shown to be less than 5%, when the latitude is below 30°(see the blue curve displayed in Figure S1 of the supporting materials).

Using the formula (8) and (37), we get

$$\tilde{b}'_{\varphi_n}(x) = \frac{iCx}{f}\tilde{b}'_{\theta_n} - \frac{im}{f}\partial_x\tilde{b}'_{\theta_n} = \frac{iCx}{f\sqrt{(1-x^2)(1+\beta^2x^2)}}y_n(x) - \frac{im}{f}\partial_x\tilde{b}'_{\theta_n} \tag{38}$$

where, $f = m^2 + (1-x^2)M(x)$.

From the formula (33), $\tilde{b}_{\varphi_n}(x)$ is expressed as follows

$$\tilde{b}_{\varphi_n}(x) = \sqrt{1-x^2}\tilde{b}'_{\varphi_n}(x) = \frac{iCx}{f\sqrt{(1+\beta^2x^2)}}y_n(x) - \frac{im}{f}\sqrt{1-x^2}\partial_x\tilde{b}'_{\theta_n} \tag{39}$$

where, $\partial_x \tilde{b}'_{\theta_n} = \frac{1}{\sqrt{(1-x^2)(1+\beta^2x^2)}}\partial_x y_n(x) - \frac{x(\beta^2-1-2\beta^2x^2)}{[(1-x^2)(1+\beta^2x^2)]^{\frac{3}{2}}} y_n(x)$, which is derived from the formula (35).

Using the series expansion approach, $\tilde{b}_{\varphi_n}(x)$ can be further expressed by

$$\tilde{b}_{\varphi_n}(x) = \frac{i}{f}\left[\frac{C}{\sqrt{(1+\beta^2x^2)}} + \frac{m(\beta^2-1-2\beta^2x^2)(1+x^2)}{(1+\beta^2x^2)^{\frac{3}{2}}}\right] x y_n(x) - \frac{im}{f\sqrt{1+\beta^2x^2}}\partial_x y_n(x) \quad (40)$$

Not that both $\tilde{b}_{\theta_n}(x)$ and $\tilde{b}_{\varphi_n}(x)$ developed here are dimensionless quantities and they essentially reflect the latitudinal distribution law of the waves. Furthermore, considering the initial time $t = t_0$, then b_{θ_n} and b_{φ_n} can be written as

$$\left.\begin{aligned} b_{\theta_n}(t_0, x, z, \varphi) &= \tilde{b}_{\theta_n}(x)\, sin(\, kz)\, exp(\, im\varphi) \\ b_{\varphi_n}(t_0, x, z, \varphi) &= \tilde{b}_{\varphi_n}(x)\, sin(\, kz)\, exp(\, im\varphi) \end{aligned}\right\} \quad (41)$$

where, $z = r - R$; $k = \frac{\pi}{H}$.

Here, at the CMB ($r = R$, i.e., $z = 0$) and the bottom of the stratified layer ($r = R - H$, i.e., $z = -H$), we give $b_{\theta_n} = b_{\varphi_n} = 0$. Therefore, to reveal the latitudinal distribution law of the waves, we define the vertically average values of the perturbed magnetic fields inside the thickness *H* as follows

$$\left.\begin{aligned} \bar{b}_{\theta_n} &= \frac{1}{H}\int_{-H}^{0} b_{\theta_n}(t_0, x, z, \varphi)dz = \tilde{b}_{\theta_n}(x)\, exp(\, im\varphi)\frac{1}{H}\int_{-H}^{0} sin(\, kz)dz \\ \bar{b}_{\varphi_n} &= \frac{1}{H}\int_{-H}^{0} b_{\varphi_n}(t_0, x, z, \varphi)dz = \tilde{b}_{\varphi_n}(x)\, exp(\, im\varphi)\frac{1}{H}\int_{-H}^{0} sin(\, kz)dz \end{aligned}\right\} \quad (42)$$

where, $-H < z < 0$.

So

$$\left.\begin{aligned} \bar{b}_{\theta_n} &= -\frac{2}{\pi}\tilde{b}_{\theta_n}(x)\, exp(\, im\varphi) \\ \bar{b}_{\varphi_n} &= -\frac{2}{\pi}\tilde{b}_{\varphi_n}(x)\, exp(\, im\varphi) \end{aligned}\right\} \quad (43)$$

Furthermore,

$$\bar{b}_{\theta_n} = Re\left(\bar{b}_{\theta_n}\right) + iIm\left(\bar{b}_{\theta_n}\right)$$

where, $\begin{cases} Re(\bar{b}_{\theta_n}) = -\frac{2}{\pi}\left\{Re\left[\tilde{b}_{\theta_n}(x)\right]\cos(m\varphi) - Im\left[\tilde{b}_{\theta_n}(x)\right]sin(m\varphi)\right\} \\ Im\left(\bar{b}_{\theta_n}\right) = -\frac{2}{\pi}\left\{Re\left[\tilde{b}_{\theta_n}(x)\right]sin(m\varphi) + Im\left[\tilde{b}_{\theta_n}(x)\right]\cos(m\varphi)\right\} \end{cases}$.

and

$$\bar{b}_{\varphi_n} = Re\left(\bar{b}_{\varphi_n}\right) + iIm\left(\bar{b}_{\varphi_n}\right)$$

where, $\begin{cases} Re(\bar{b}_{\varphi_n}) = -\frac{2}{\pi}\left\{Re\left[\tilde{b}_{\varphi_n}(x)\right]\cos(m\varphi) - Im\left[\tilde{b}_{\varphi_n}(x)\right]sin(m\varphi)\right\} \\ Im\left(\bar{b}_{\varphi_n}\right) = -\frac{2}{\pi}\left\{Re\left[\tilde{b}_{\varphi_n}(x)\right]sin(m\varphi) + Im\left[\tilde{b}_{\varphi_n}(x)\right]\cos(m\varphi)\right\} \end{cases}$

Here, real parts of $\bar{b}_{\theta_n}$ and $\bar{b}_{\varphi_n}$ (i.e., $Re(\bar{b}_{\theta_n})$ and $Re(\bar{b}_{\varphi_n})$) are considered and their

results are further displayed in Figure 6, which generally shows the low-latitude distribution features and the equatorially symmetry or anti-symmetry property. Moreover, Figure 6 also shows that the results of $Re(\bar{b}_{\theta_n})$ (n=0,1) and $Re(\bar{b}_{\varphi_n})$ (n=1,2) can well present in the low-latitude regions below 30 degrees, yet the results of modes (n=2,3) for $Re(\bar{b}_{\theta_n})$ can extend to the higher latitude (i.e., >30 degrees) regions. As to the results that exceed to the higher latitude (e.g., >30°), they might not accurately reflect the real situation due to the relatively larger errors, but we suggest that the perturbed magnetic field models (see formulas (37) and (40)) are still significant to understand the origins and the spatial features of the observed equatorial waves in light of the following (at least) two points (here, taking Figure 6 (f) for example),

1) Figure 6 (f) shows the spatial distribution feature of the azimuthal perturbed magnetic field b_φ (n=1), which is shown to be mainly confined to the equatorial regions between latitude 15°N and S. Since b_φ couples to the core surface azimuthal flow v_φ, meaning that v_φ also presents the same feature as that of b_φ (see the section 4.3). Meanwhile, the observed core surface azimuthal flow acceleration (i.e., $\frac{\partial v_\varphi}{\partial t}$) just locate at the same regions with the latitude below 15° (see the Figure 6(i) cited from Kloss and Finlay, 2019), the profile of which is similar to that of Figure 6(f).

2) Importantly, within the latitude $\pm$15°, the discarded term $O(x^4)$ in formula (B8) only accounts for (less than) 2% of the remaining parts (see Figure A4), meaning that the models developed here can own the high enough accuracy (the relative errors are smaller than 1%, see Appendix C) to describe the observed equatorial waves occurring in the regions with latitude below 15 degrees.

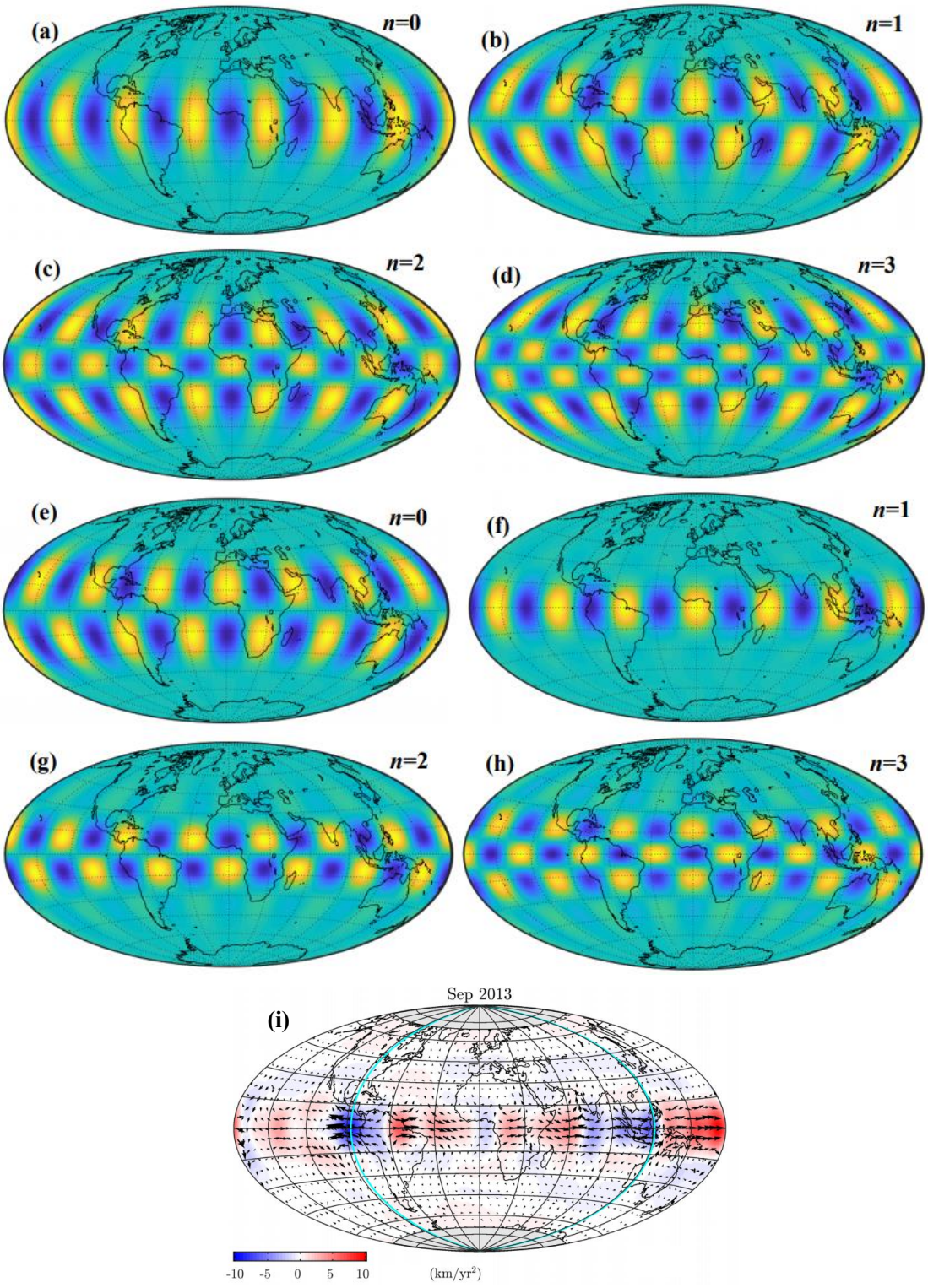

631

632

633 **Figure 6**. Results of the perturbed magnetic field models and the observed azimuthal core flows. Spatial

634 distribution of the perturbed magnetic fields ($Re(\bar{b}_{\theta_n})$ and $Re(\bar{b}_{\varphi_n})$, n=0, 1, 2, 3) at the initial time ($t = t_0$),where (a), (b), (c) and (d) show $Re(\bar{b}_{\theta_n})$; (e), (f), (g) and (h) display $Re(\bar{b}_{\varphi_n})$; (i) shows the result of the

636 observed azimuthal core surface flow acceleration (i.e., $\frac{\partial v_\varphi}{\partial t}$) cited from Kloss and Finlay (see their Figure 13).

637

4. Discussion

Theoretical studying the properties of the eMAC waves and detection of them from the potential observation sources (e.g., the geomagnetic field changes) are significant to solve the controversial issue that whether the FOC is stratified or not, since the existence of these waves itself implies a strongly stratified layer existing atop the Earth's core. The observed equatorially hydromagnetic waves propagating eastward in the vicinity of 8.5yr period (Chi-Durán et al, 2020) may just represent the eMAC waves, since the properties (e.g., the equatorial confinement, eigen-period, propagation velocity and direction) of the eMAC waves can match the observations. Nevertheless, it is still required to further justify whether the results of the eMAC wave model studied in this work are reasonable and self-consistent. Here, we need to ensure that the following two relationships are valid.

Relationship 1: $I \ll M$.

Proof is as follows: Here, we give the complete forms of I and M. According to the formula (7), $I = \frac{\tilde{\omega}^2 k^2 R^2}{N^2}$, so we can write it as

$$I = Re(I) + i\,Im(I)$$

where, $Re(I) = \frac{k^2R^2}{N^2}(\omega^2 - \alpha^2)$; $Im(I) = \frac{2k^2R^2}{N^2}\alpha\omega$.

Additionally, from the appendix A, M is written as

$$M = Re(M) + i\,Im(M)$$

where, $Re(M) = \frac{V_a^2 k^4 R^2[\omega^2+(\alpha^2+\alpha\eta k^2)]}{N^2[\omega^2+(\alpha+\eta k^2)^2]}$; $Im(M) = -\frac{\omega\eta R^2 V_a^2 k^6}{N^2[\omega^2+(\alpha+\eta k^2)^2]}$.

Using $\alpha = -\eta k^2\gamma$, here γ =0.95, 20km<H<100km, T=8.5yr, we can estimate

$$\frac{(\alpha+\eta k^2)^2}{\omega^2} = \frac{(\eta k^2)^2(1-\gamma)^2}{\omega^2} = \frac{\pi^2T^2(1-\gamma)^2}{4H^4\mu^2\sigma^2} < 0.0017$$

$$\left|\frac{\alpha^2+\alpha\eta k^2}{\omega^2}\right| = \frac{(\eta k^2)^2\gamma(1-\gamma)}{\omega^2} = \frac{\pi^2T^2\gamma(1-\gamma)}{4H^4\mu^2\sigma^2} < 0.03$$

So, $(\alpha+\eta k^2)^2 \ll \omega^2$ and $|\alpha^2+\alpha\eta k^2| \ll \omega^2$.

Thus, $Re(M)$ and $Im(M)$ are further simplified as

$$Re(M) = \frac{V_a^2 k^4 R^2}{N^2},\ Im(M) = -\frac{\eta R^2 V_a^2 k^6}{N^2\omega}$$

Here, V_a =0.0048m/s, 20km<H<50km, T=8.5yr, we can obtain

$$\left|\frac{Re(I)}{Re(M)}\right| = \frac{\omega^2-\alpha^2}{V_a^2k^2} < \frac{\omega^2}{V_a^2k^2} = \frac{4H^2}{V_a^2T^2} < 0.006$$

$$\left|\frac{Im(I)}{Im(M)}\right| = \frac{2\omega^2\gamma}{V_a^2k^2} = \frac{8\gamma H^2}{V_a^2T^2} < 0.01$$

So

$$|Re(I)| \ll |Re(M)| \text{ and } |Im(I)| \ll |Im(M)|$$

Finally, the relationship 1 (i.e., $I << M$) is proved.

Relationship 2: $|Im[M(0)]| \ll \left|Im[\frac{mC}{M(x)}]\right|$ and $|Im[\beta^2 M(0)]| \ll \left|Im[\frac{C^2}{M(x)}]\right|$.

Note that the relationship 2 is required to derive the equation (10), the detailed information of which can be seen in the Appendix A. Using the related parameters (Table 1) and the damping rate derived by this work, we can show that the relationship 2 is valid.

Proof is as follows: According to the Appendix A, we can write the following formulas

$$\left|\frac{Im(M(0))}{Im(\frac{mC}{M(x)})}\right| = \frac{\omega\eta R^2 V_a^4 k^8}{2\Omega m N^2(\alpha+\eta k^2)[\omega^2+(\alpha+\eta k^2)^2]}$$

$$\left|\frac{Im(\beta^2 M(0))}{Im(\frac{C^2}{M(x)})}\right| = \frac{\eta\beta^2 V_a^4 k^6}{4\Omega^2(2\alpha+\eta k^2)[\omega^2+(\alpha+\eta k^2)^2]}$$

where, $\alpha = -\eta k^2\gamma$.

Adopting the related parameters (e.g., γ =0.95, *H*=30km, *N*=10Ω, V_a =0.0048m/s), we estimate that $\left|\frac{Im(M(0))}{Im(\frac{mC}{M(x)})}\right|$~ 0.007, $\left|\frac{Im(\beta^2 M(0))}{Im(\frac{C^2}{M(x)})}\right|$~0.003. Therefore, the relationship 2 is proved.

4.1. Stratified parameters required by the eMAC waves

This work mainly considers the parameter *N* being in the range of 7~15Ω suggested by Helffrich and Kaneshima (2010). What is sure is that, when *N*≥7Ω, we can present the stable and logically self-consistent results. As discussed above, when *N*≥7Ω, we can estimate $\gamma \to 1$ (Figure 2), which further simplifies the calculation of the eigen-period, while we know that $\gamma \neq 1$ (since $A_n \neq B_n$) from the formula (22), which makes the above relationship 2 be valid. Given that the exact *N* value is still uncertain, for example, Gastine et al (2019) computed the geodynamo models by varying it from 0 to 50Ω. Here, we would like to further discuss the case of the smaller *N* values.

Figure 7 presents the γ values (1Ω≤ N ≤15Ω), showing that a threshold N_0 exists. If $N > N_0$, the γ value can quickly approach to 1 with the increase of *H*, where N_0 is close to 5Ω (see the green curves in Figure 7), which, of course, is an approximate value; if $N < N_0$, the γ values

will change more slowly with H increase. If γ is not close to 1, one will encounter a more complicate situation, that is, the $\tilde{F}_n$ term in formula (24) cannot be displaced by the F_n term, for example, if γ =0.6, then $\frac{T_1}{F_n}$~0.15, which means that T_1 can be comparable with F_n, so T_1 cannot be removed from the formula (24). In this case, the equation (23) (i.e., $\tilde{D}_n\omega^2 + \tilde{E}_n\omega + \tilde{F}_n = 0$) no longer represents a simple quadratic equation with respect to ω, nevertheless, this work does not concern this case too much, as it is not impossible for the core surface to have a strong stratified layer (e.g., N>5Ω), which makes the γ value be close to 1.

Many works (e.g., Gubbins and Davies, 2013; Buffett, 2014; Christensen, 2018) indicated that when the location is closer to the CMB, the value of N will be larger. Considering the estimated H values in this work are only 21~35km (from the lower degrees, n=0,1,2,3), which is very close to the CMB, so N may reach its maximum value, i.e., N_{max} with the potential amplitude of ~20Ω at the CMB (Gubbins and Davies, 2013). Even though these estimated H values (i.e., 21~35km) are quite small, the existence of such a thin layer is still physically plausible, since it may reflect a sublayer within the broader stratification region as suggested by BM19, and this thin layer formation may be due to the accumulation of the light elements at the CMB under the action of barodiffusion (e.g., Gubbins and Davies, 2013).

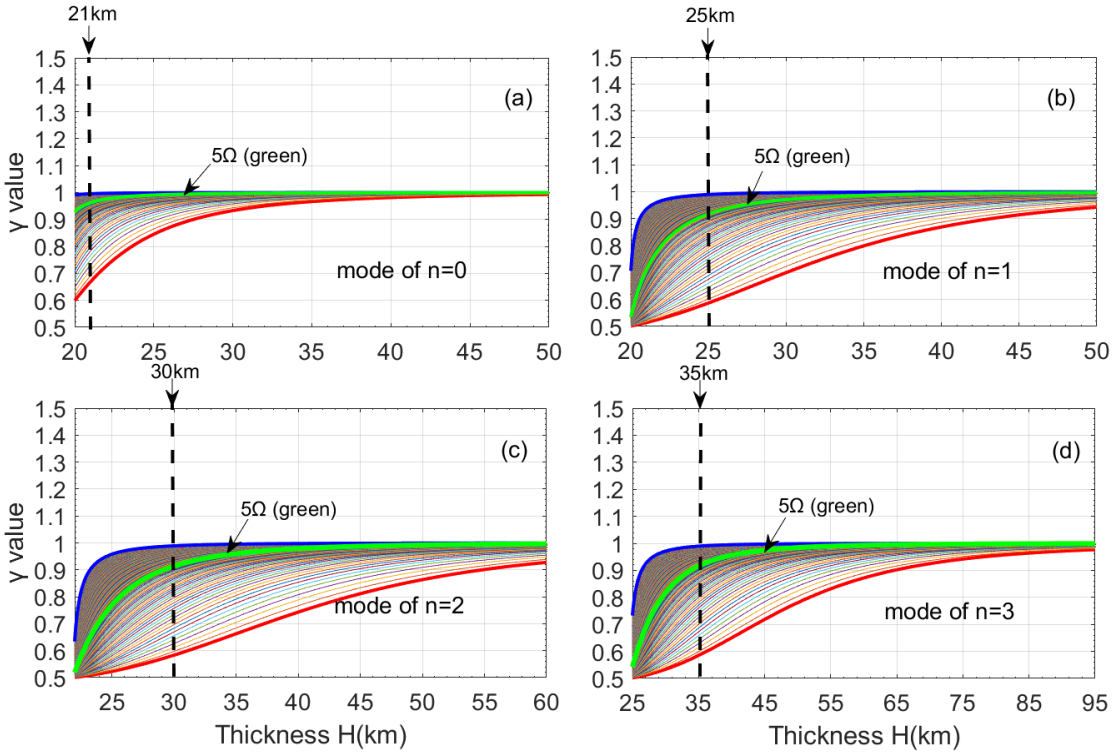

Figure 7. The γ values change with N and H (Varying N from 1Ω to 15Ω). The blue curves show the upper

boundary (representing the case N=15Ω), the red curves display the lower boundary (representing the case N=1Ω), the interval between the two adjacent curves is 0.1Ω; the vertical black dashed lines show the H values (see Figure 3) estimated by the eMAC waves with the 8.5yr eigen-period.

Besides, BM19 only considered the first two modes (i.e., n=0,1) of the eMAC waves and they suggested that the H value is less than 30km when the waves own the periods less than 10yr. This work further presents the related analytical model with any degree n (the first four degrees, i.e., n=0,1,2,3, are considered), the results show that the larger H values can be estimated from the higher degree modes ($n \geq 3$) with the 8.5yr period, e.g., when n=3, H is ~35km. As for the model accuracy, we find that the relative errors can be less than 5%, when the latitude is below 25 degrees. Nevertheless, the eMAC waves with the higher degrees (e.g., $n \geq 3$) are more likely to extend to the higher latitude regions (see Figure 6) with latitude >30 degrees, though the eMAC waves can generally show the equatorial confinement property. Considering the results of the developed eMAC wave model may extend to the relatively higher latitude regions based on the parameters listed in Table 1, so we need to further discuss the potential physical factors that can increase the low-latitude confinement degree.

4.2. Equatorial confinement influenced by the radial magnetic field at the CMB

As mentioned above, it is important for the MAC waves to own the equatorial confinement property, which can theoretically determine the existence of the so-called eMAC waves. Here, we will further discuss the physical factors which can influence this property. According to the section 3.3, the equatorial confinement property depends on the parameter $\tilde{\alpha}$, which is related to the following factors, i.e., ρ_0, m, β, $B_r(0)$ and the stratification parameters (N, H). Here, ρ_0=1.1×10^{4}kgm^{-3} being the core density, which has been widely used; m=7 being the spatial wave number of the observed eastward propagating waves, which is inferred from the wavelength of variations in the time-longitude plot of geomagnetic filed acceleration at the CMB (see Chi-Durán et al, 2020). Here, we consider the two parameters (i.e., ρ_0, m) as the well-known factors. As for the parameter β, it can be taken as an adjustable parameter, the value of which (~1.58, see Table 1) is estimated by fitting a geodynamo model (Christensen and Aubert, 2006). In the section 3.3, we have shown the influence of β on the equatorial confinement, here $B_r(0)$

will be further considered to discuss the equatorial confinement of the waves.

Actually, $B_r(0)$~0.48mT (see Table 1) is also an adjusted result to match the rms value of the radial magnetic field at the CMB inferred from the geodetic observations (i.e., B_r^{rms}~0.65mT), see BM19. The exact value of $B_r(0)$ is still not well known. For example, from the aforementioned geodynamo model, B_r^{rms}~0.24mT is estimated, meaning that the smaller value of $B_r(0)$ (<0.24mT) is required to match this value. Therefore, we also adjust $B_r(0)$ (by varying it from 0.1mT to 0.5mT) to show its potential influences on the equatorial confinement. Figure 8 shows that $B_r(0)$ can obviously affect the confinement degree, especially, the weaker the $B_r(0)$ (<0.5mT) is, the greater degree of the confinement will be, since the weaker $B_r(0)$ can result in the larger $Re(\tilde{\alpha})$ (see Figure 9), and thus increase the equatorial confinement. Additionally, we can obtain $Im(\tilde{\alpha}) \ll Re(\tilde{\alpha})$ from Figure 9, hence we only need to consider $Re(\tilde{\alpha})$ to study the confinement property.

In summary, our results show that, besides the gradient strength (characterized by the factor β), the weaker $B_r(0)$ also can increase the equatorial confinement degree. That is to say, the joint effects of the two factors (i.e., the larger β value and the weaker $B_r(0)$) can significantly increase the equatorial confinement of the waves. Moreover, the result from the joint effects is shown in Figure 10 (taking the b_{θ_n} for example), which shows the greater confinement degree compared to Figure 6. Here, $B_r(0)$ is set to be 0.2mT, while β is set to be 3.46 (which is larger than 1.58). Further using $B_r(x) = B_r(0)\sqrt{1+\beta^2 x^2}$, we can estimate $B_r(\pm 1)$~0.72mT (at the two poles). Note that these parameter values shown here are appropriate as they are generally well consistent with the observed palaeomagnetic time-average radial magnetic field at the core surface (with the amplitude ~0.6mT near the poles, see the Figure 3 in Jackson, 2003) and the results from the numerical geodynamo model (with the amplitude ~0.75mT, see the Figure 3 in BM19).

The above discussion coincides with the previously thought, i.e., the strong gradient strength of the magnetic force can produce the so-called wave guide, which further results in the appearance of the equatorial confined features. Nevertheless, differing from the previous work, we further highlight the joint effects of the two factors (i.e., β and $B_r(0)$).

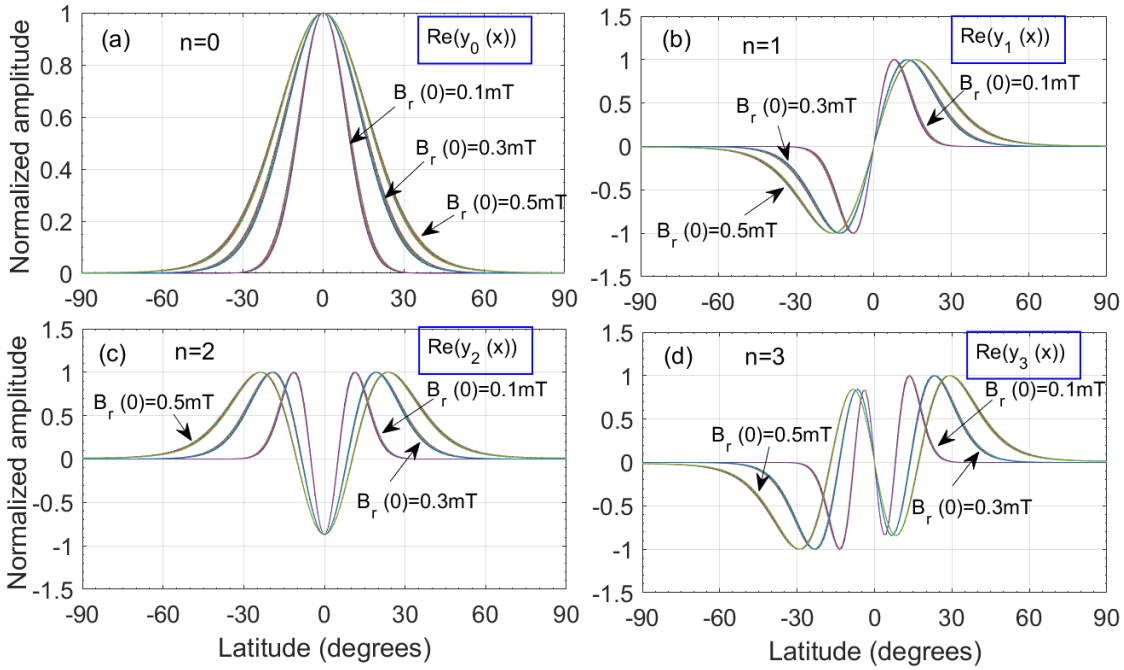

Figure 8. Influence of radial magnetic field at the CMB equator on the confinement degree (here, $7\Omega \leq N \leq 15\Omega$, H=25km, β=1.58). three cases (i.e., $B_r(0)$=0.1mT, 0.3mT and 0.5mT) are displayed. The smaller $B_r(0)$ value can result in the greater confinement degree.

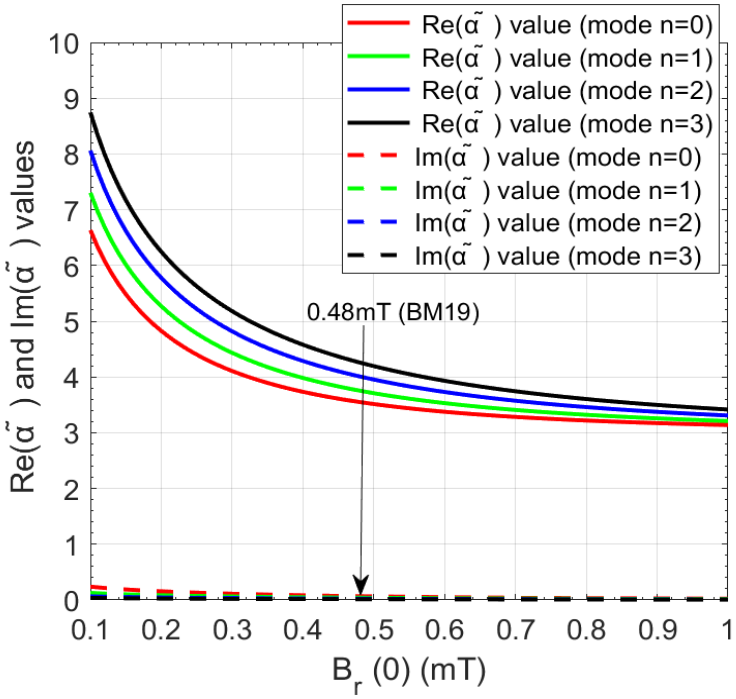

Figure 9. Influence of the radial magnetic field at the CMB equator on the $\tilde{\alpha}$ values. The vertical arrow shows the values of $Re(\tilde{\alpha})$ and $Im(\tilde{\alpha})$, when $B_r(0)$ is adopted to be 0.48mT.

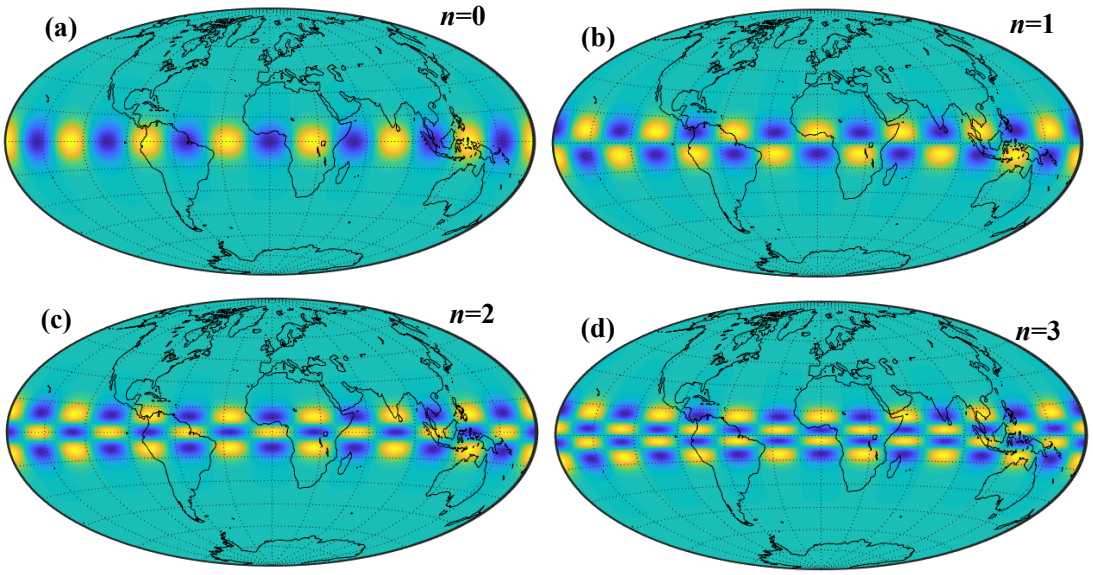

Figure 10. Spatial distribution of the perturbed magnetic fields $Re(\bar{b}_{\theta_n})$ (here, n=0, 1, 2, 3) at the initial time ($t = t_0$). Here, $B_r(0)$=0.2mT, β=3.46, H=25km, N=10Ω.

4.3. Preliminary discussing the possibility of the axial AM carried by eMAC waves

Given that the eigen-periods of the eMAC waves can match the observed ~8.6yr period in LOD changes, a scientific question that whether the eMAC waves can be a potential source to excite the LOD changes may arise. Hence, it is necessary to theoretically discuss the possibility of the eMAC waves carrying the axial angular momentum (AM). Actually, the eMAC waves can be seen as the eigen-modes of FOC stratification system, so the generation of these waves essentially depends on the information of the excitation sources. However, to our current knowledge, the detailed information about the excitations is still not well-known. As Gillet et al (2021) suggested, it remains a challenge to examine the exact excitation sources leading to the eMAC waves. If the related excitation sources are uniformly distributed within the global range, then the eMAC waves may present the rigorously periodic feature along the longitude direction on the global scale, which is similar to the profile shown in Figure 6. If it is this case, the eMAC waves cannot carry any axial AM, because, in this case, the axial AM will be counterbalance.

However, the reality may be not like this. The actual AM cannot be canceled out, since the appearance of eMAC waves is more likely to present the significantly localized features. The modern geomagnetic observations (e.g., Finlay et al,2016; Chi-Durán et al, 2020) may just provide

798 the observed evidences to support this point. For example, Finlay et al (2016) indicated that the
799 most prominent feature of the secular acceleration of radial geomagnetic field at the core surface
800 is positive-negative pair under the areas of India-South East Asia and northern south America;
801 while Chi-Durán et al (2020) further detected the ~8.73yr periodic equatorially eastward
802 propagating travelling waves mainly from the Southeast Asia area (see Figure 11). In addition,
803 both the equatorial waves and the LOD changes have the same ~8.6yr periodic component. These
804 observed phenomena imply that the eMAC waves may carry the axial AM.

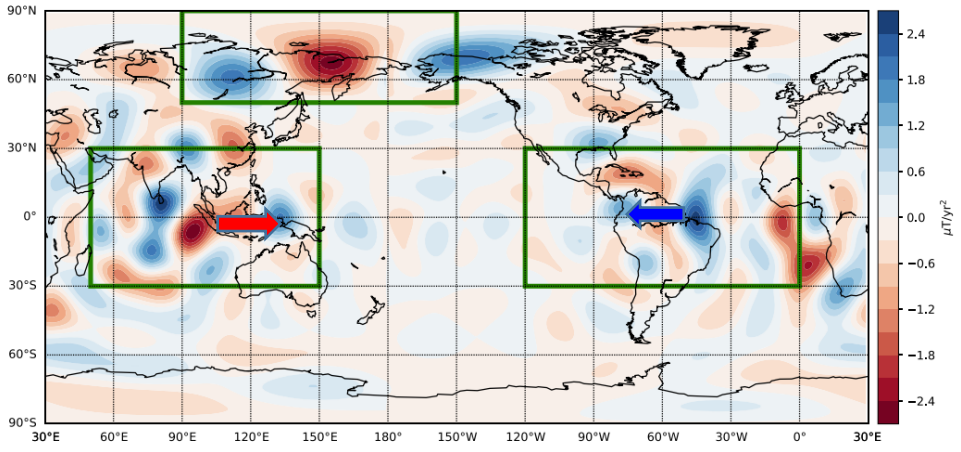

805

806 **Figure 11**. Secular acceleration of the geomagnetic field at 2011 (cited from Chi-Durán et al,2020). The red and
807 blue arrows (respectively expresses the eastward and westward propagation) are added by us to clearly display the
808 propagation directions of the observed fast equatorial waves, where these waves locating at the Southeast Asia area
809 and the Atlantic area respectively own ~8.73yr and ~7.1yr periods.

810

811 Since the axial AM changes depend on the azimuthal fluid core motions, so we need to
812 discuss the azimuthal core flows induced by the eMAC waves. According to the coupling between
813 the perturbed azimuthal magnetic field b_φ and the azimuthal fluid core motions (denoted by v_φ),
814 i.e., $\frac{\partial v_\varphi}{\partial z} = -\frac{i\tilde{\omega}\chi b_\varphi}{B_r}$ (see the Appendix equation (A14) in BM19), her we can directly give the v_φ
815 model as follows

816 $$v_\varphi = \frac{i\tilde{\omega}\chi}{k}\frac{\tilde{b}_\varphi(\theta)}{B_r}[1+\cos(kz)]e^{i(m\varphi-\tilde{\omega}t)} \quad (44)$$

817 where, v_φ satisfies the boundary condition, i.e., $v_\varphi = 0$ at the base of the layer (i.e., $z = -H$);
818 $\tilde{\omega} = \omega + i\alpha$.

819 Formula (44) owns the form of $e^{-i\tilde{\omega}t}(= e^{\alpha t}e^{-i\omega t})$, which reflects a typical damping
820 oscillation mode (corresponding to the longitude φ). However, the observed azimuthal flow

velocity (denoted by v_φ^{obs}) due to the eMAC waves cannot be simply described by the formula (44), the reason of which is as follows: The forced response of the waves to a local excitation source should be expressed as a linear combination of global waves, the appearance of the eMAC waves could be the result of the linear superposition of the eigen-modes of the waves on the planetary scales, this approach is routinely used in seismology to construct seismograms for a localized earthquake, based on a linear combination of (global) normal modes (see Gilbert, 1970); consequently, the v_φ^{obs} field (on the global scale) should be due to the superposition of the excited waves related to the excitation source information, meaning that the amplitude of v_φ^{obs} should change with the longitude φ on the whole planetary scales (see Figure 6(i)), which, however, cannot be shown by the above expression of v_φ, which shows a constant amplitude unrelated to φ.

Nevertheless, the spatial distribution features of the observed eMAC waves indeed can be reflected by the form of v_φ, that is, along the vertical and latitudinal directions, v_φ^{obs} should own the similar mathematical form as that of v_φ. Here, we can construct the v_φ^{obs} field model as following

$$v_\varphi^{obs} = A(\varphi)\tilde{b}_\varphi(\theta)[1+\cos(kz)]e^{i(m\varphi-\tilde{\omega}t)} \tag{45}$$

where, $A(\varphi)$ is an undetermined function with unite 'm/s', which reflects the amplitude of the waves change with φ resulting from the superposition of the excited waves on the global scales; $\tilde{b}_\varphi(\theta)$ (dimensionless) reflects the latitudinal distribution characteristics of the observed waves; $[1+\cos(kz)]$ reflects the vertical distribution feature; the part of $e^{im\varphi}e^{-\tilde{\omega}t}$ shows the property of the wave motion.

Furthermore, the axial AM (i.e., L_{axial}) carried by the eMAC waves is written by

$$L_{axial} = \int_V \rho_0 v_\varphi^{obs} r\,sin\,\theta\,dV \tag{46}$$

where, ρ_0 refers to the core density inside the stratified layer; $dV = r^2\,sin\,\theta\,drd\theta d\varphi$.

Formula (46) shows that v_φ^{obs} can cause L_{axial} and further probably induce the LOD changes, under the action of the electromagnetic coupling effects at the CMB. Obviously, to obtain the L_{axial}, the issue is to determine v_φ^{obs}. In the formula (45), the expression of $\tilde{b}_\varphi(\theta)$ has been theoretically given (see the formula (39)), so the next step is to give $A(\varphi)$, which might be inferred from the current core flow model (e.g., Kloss and Finlay, 2019), however, the further study is beyond the scope of this work.

Of course, the totally axial AM induced by the eMAC waves confined to the stratified layer at the top of the core, neglecting coupling to the bulk of the deep core, may be so small that the eMAC waves might not cause the LOD changes to the detectable level, but a quantitative discussion on this would be worthy study in future.

5. Conclusions

In this work, we carefully derive the 'Weber equation' (i.e., the formula (12)) and its specific solution (i.e., formula (18)) to determine the time-spatial scales on which they are reliable to describe the changes of the perturbed magnetic field with latitude. To obtain the 'Weber equation', besides some small quantities are ignored, which are shown to be (at least) two orders of magnitude weaker than the remaining terms (see Appendix A and the discussion part), the so-called truncation treatment (i.e., removing the $O(x^4)$ terms, which depend on the latitude, see Appendix B) is also made. We find that, when the latitude is below 15 degrees (where the observed non-zonal azimuthal core surface flows can appear, see Kloss and Finlay, 2019), the discarded term (i.e., $O(x^4)$) only accounts for (less than) 2% of the remaining parts (see Figure A4), meaning that the relative errors of the results caused by the truncation treatment is smaller than 2% (see the Appendix C). Moreover, even though the $O(x^4)$ terms account for 10% (corresponding to the latitude 25°), the relative errors are still small, i.e., ~5%.

Furthermore, using the 'Weber equation' (i.e., the formula (12)) and its specific solution (i.e., formula (18)), we can give the systematically physical expressions of representing the relevant properties (i.e., the equatorial confinement, damping rate, eigen-period, propagating velocity) and the perturbed magnetic field models, where the buoyancy frequency N is required to be larger than a threshold N_0, which is close to be 5Ω. The related results are briefly summarized as follows:

1) We present the analytical formula, i.e., $y_n(x) = A_n e^{-\frac{1}{2}\tilde{\alpha}^2 x^2} H_n(\tilde{\alpha}x)$, to represent the latitudinal distribution law of the MAC waves. Here, $H_n(\tilde{\alpha}x)$ being the Hermite polynomial term of the degree n, which implies that the MAC waves have the equatorially symmetric and antisymmetric characteristics, while the equatorial confinement degree is determined by $\tilde{\alpha}$, which depends on the joint effects from the (not well-known) physical parameters, i.e., β and $B_r(0)$. Besides the parameter β suggested by BM19, the influence on the equatorial confinement from

$B_r(0)$ is also discussed, showing that the weaker $B_r(0)$ (<0.5mT) also can obviously increase the confinement degree.

2) This work shows that the damping rate α of the eMAC waves can be estimated by $\alpha \approx -\frac{\pi^2}{\mu\sigma H^2}$, meaning that the damping effects mainly depend on σ and H^2. Therefore, detection of the damping effects of the eMAC waves will be helpful to infer the information of the electrical conductivity and the stratification atop the Earth's core. Additionally, the *H* value is predicted to be 21~35km, when the eigen-periods of the eMAC waves with the degrees (e.g., *n*= 0,1,2,3) match the 8.5yr period.

3) The azimuthal perturbed magnetic field model b_φ with degree *n*=1 (see Figure 6(f)) is shown to be mainly confined to the equatorial regions with latitude below 15 degrees, the profile of which is generally consistent with that of the observed core surface azimuthal flows (see Kloss and Finlay, 2019).

In summary, the results of this work are significant to deeply understand the origins of the observed equatorial waves, their physical properties and the dynamics of the Earth's equatorial regions.

Acknowledgments

This work is supported by the B-type Strategic Priority Program of the Chinese Academy of Sciences (Grant No. XDB41000000), Youth Innovation Promotion Association CAS (2021259) and National Natural Science Foundation of China (grant No. 11803064, 41774017).

Data Availability Statement

The related core stratification data is available through Helffrich and Kaneshima (2010); the observed core wave parameter data is available through Chi-Durán et al (2020); the observed LOD data is available from the IERS website (https://www.iers.org/IERS/EN/Data Products/Earth Orientation Data/eop.html).

Appendix

Appendix A: On the derivation of formula (10).

Actually, from the formula (8), we can rigorously derive the following equation (A1) (the detailed derivation process is shown in the Supporting Materials), which is different from the formula (10) (i.e., the formula (44) in BM19).

$$(1-x^2)\partial_x^2\tilde{b}'_\theta - 2x(\frac{1-\beta^2+2\beta^2x^2}{1+\beta^2x^2})\frac{m^2}{f}\partial_x\tilde{b}'_\theta + [\underbrace{\frac{C^2x^2}{M(x)}}_{1} + \underbrace{\frac{mC}{M(x)} - M(x)}_{2} - \underbrace{\frac{m^2}{1-x^2}}_{3} + \underbrace{\frac{2m(1-\beta^2+2\beta^2x^2)x^2}{(1+\beta^2x^2)}\frac{C}{f}}_{4}]\tilde{b}'_\theta = 0 \quad \text{(A1)}$$

where, $C = \frac{2\Omega k^2R^2}{N^2}\tilde{\omega}$, $\tilde{\omega} = \omega + i\alpha$, $i^2 = -1$, $M(x) = \frac{V_a^2k^4R^2}{\chi N^2}$, $\chi = 1 + \frac{i\eta k^2}{\tilde{\omega}}$, $f = m^2 + (1-x^2)M(x)$.

Here, $M(x)$ and f are respectively expressed by

$$\begin{cases} M(x) = \frac{V_a^2k^4R^2\tilde{\omega}}{N^2(\tilde{\omega}+i\eta k^2)} = \frac{V_a^2k^4R^2}{N^2[\omega^2+(\alpha+\eta k^2)^2]}[(\omega^2+\alpha^2+\alpha\eta k^2) - i\omega\eta k^2] \\ f = m^2 + (1-x^2)M(x) = \frac{N^2m^2(\tilde{\omega}+i\eta k^2)+(1-x^2)V_a^2k^4R^2\tilde{\omega}}{N^2(\tilde{\omega}+i\eta k^2)} \end{cases} \quad \text{(A2)}$$

In order to further show that how to carefully obtain the equation (10), we need to consider every term in formula (A1). Here, defining

$$T_1(x) = \frac{C^2x^2}{M(x)};\ T_2(x) = \frac{mC}{M(x)} - M(x);\ T_3(x) = \frac{m^2}{1-x^2};\ T_4(x) = \frac{2m(1-\beta^2+2\beta^2x^2)x^2}{(1+\beta^2x^2)}\frac{C}{f}.$$

Then, we can calculate the $\frac{C}{f}$ term in $T_4(x)$

$$\frac{C}{f} = 2\Omega k^2R^2\frac{\tilde{\omega}(\tilde{\omega}+i\eta k^2)}{N^2m^2(\tilde{\omega}+i\eta k^2)+(1-x^2)V_a^2k^4R^2\tilde{\omega}}$$

$$= \frac{2\Omega k^2R^2\tilde{\omega}(\tilde{\omega}+i\eta k^2)}{N^2\{\omega\left[m^2+(1-x^2)\frac{V_a^2k^4R^2}{N^2}\right]+i[m^2(\alpha+\eta k^2)+\alpha(1-x^2)\frac{V_a^2k^4R^2}{N^2}]\}}$$

$$= \frac{2\Omega k^2R^2}{N^2}\frac{\tilde{\omega}(\tilde{\omega}+i\eta k^2)}{\omega\left[m^2+(1-x^2)\frac{V_a^2k^4R^2}{N^2}\right]+i\{\alpha\left[m^2+(1-x^2)\frac{V_a^2k^4R^2}{N^2}\right]+m^2\eta k^2\}}$$

Adopting H>15km, $N \geq 7\Omega$, $V_a = \frac{B_r}{\sqrt{\mu\rho_0}}$~0.0041m/s, one can estimate that $\frac{V_a^2k^4R^2}{N^2}$ <1.5, especially, when H>20km, one can obtain that $\frac{V_a^2k^4R^2}{N^2}$<0.47$\ll m^2$ (=49), thus $(1-x^2)\frac{V_a^2k^4R^2}{N^2} \leq \frac{V_a^2k^4R^2}{N^2} \ll m^2$. Therefore

$$\frac{C}{f} = \frac{2\Omega k^2R^2}{N^2m^2}\frac{\tilde{\omega}(\tilde{\omega}+i\eta k^2)}{\omega+i(\alpha+\eta k^2)} = \frac{2\Omega k^2R^2}{N^2m^2}\tilde{\omega} \quad \text{(A3)}$$

Here, we respectively write $T_1(x)$, $T_2(x)$, $T_3(x)$ and $T_4(x)$ in terms of

$$T_1(x) = \frac{N^2x^2}{V_a^2k^4R^2}C^2\chi = \frac{4\Omega^2R^2x^2}{V_a^2N^2}[(\omega^2-\alpha^2-\alpha\eta k^2) + i(2\alpha\omega+\eta k^2\omega)] \quad \text{(A4)}$$

$$T_2(x) = \frac{mN^2}{V_a^2k^4R^2}C\chi - M(x) = \{\frac{2\Omega m}{V_a^2k^2}\omega - \frac{V_a^2k^4R^2(\omega^2+\alpha^2+\alpha\eta k^2)}{N^2[\omega^2+(\alpha+\eta k^2)^2]}\} + i\{\frac{2\Omega m}{V_a^2k^2}(\alpha+\eta k^2) + \frac{V_a^2k^6R^2\omega\eta}{N^2[\omega^2+(\alpha+\eta k^2)^2]}\} \quad \text{(A5)}$$

$$T_3(x) = \frac{m^2}{1-x^2} + i0 \quad \text{(A6)}$$

$$T_4(x) = \frac{4\Omega k^2 R^2 (1-\beta^2+2\beta^2 x^2) x^2}{N^2 m(1+\beta^2 x^2)} (\omega + i\alpha) \quad \text{(A7)}$$

In order to compare the above quantities, we define the following four ratio factors, i.e., r_i $(i = 1,2,3,4)$:

$$r_1 = \frac{Re(T_4)}{Re(T1)},\ r_2 = \frac{Re(T_4)}{Re(T2)},\ r_3 = \frac{Re(T_4)}{Re(T3)},\ r_4 = \frac{Im(T_4)}{Im(T2)}$$

Here, the possible relationship between the damping effects and the eigen-frequency ω is required to be discussed. According to the formula (6), the eMAC waves own the form of $e^{\alpha t} e^{i\omega t}$ (here α<0), which means that the free modes represent the typical damping decaying oscillations. The corresponding relaxation time τ is expressed by $\tau = -\frac{1}{\alpha}$ (namely $\alpha = -\frac{1}{\tau}$), here the appearance of these eMAC waves requires that τ should not be too short, otherwise, these waves cannot effectively appear due to the strong ohmic dissipation. We can consider that the real part of $\tilde{\omega}$ $(= \omega + i\alpha)$ is larger than the imaginary part, that is, $\omega\left(= \frac{2\pi}{T}\right) > |\alpha|(= \frac{1}{\tau})$, so $\tau > \frac{T}{2\pi}$. Focusing on the eigen-periods in the vicinity of 8.5yr, τ is required to be larger than 1yr. Furthermore, we estimated the values of r_i $(i = 1,2,3,4)$ varying τ from 2yr to 20yr, which are displayed in Figure A1, from which, we can conclude that $|r_i| \to 0$, which are much smaller than 1, that is

$$|Re(T_4)| \ll |Re(T1)|,\ Re(T_4) \ll Re(T2),\ Re(T_4) \ll Re(T3) \text{ and } Im(T_4) \ll Im(T2).$$

According to these results, it is valid to remove the fourth term (i.e.,$\frac{2m(1-\beta^2+2\beta^2 x^2)x^2}{(1+\beta^2 x^2)}\frac{C}{f}$) from the formula (A1), thus we have

$$(1-x^2)\partial_x^2 \tilde{b}'_\theta - 2x(\frac{1-\beta^2+2\beta^2 x^2}{1+\beta^2 x^2})\frac{m^2}{f}\partial_x \tilde{b}'_\theta + [\frac{C^2 x^2}{M(x)} + \frac{mC}{M(x)} - M(x) - \frac{m^2}{1-x^2}]\tilde{b}'_\theta = 0$$

Moreover, we can show that $|M(x)| \ll m^2$ (as suggested by BM19), thus $\frac{|M(x)|}{m^2}(1-x^2)$ is much smaller than 1, so $\frac{m^2}{f}$ $(= \frac{1}{1+\frac{M(x)}{m^2}(1-x^2)} \to 1)$ can be further removed. Therefore, we obtain the following equation

$$(1-x^2)\partial_x^2 \tilde{b}'_\theta - 2x(\frac{1-\beta^2+2\beta^2 x^2}{1+\beta^2 x^2})\partial_x \tilde{b}'_\theta + [\frac{C^2 x^2}{M(x)} + \frac{mC}{M(x)} - M(x) - \frac{m^2}{1-x^2}]\tilde{b}'_\theta = 0 \quad \text{(A8)}$$

Of course, we have $|M(x)| << \frac{m^2}{1-x^2}$. If directly removing $M(x)$ from the formula (A8), we can reproduce the equation (10). Nevertheless, here, we need to further compare the $M(x)$ term with the other two quantities (i.e., $\frac{C^2 x^2}{M(x)}$, $\frac{mC}{M(x)}$).

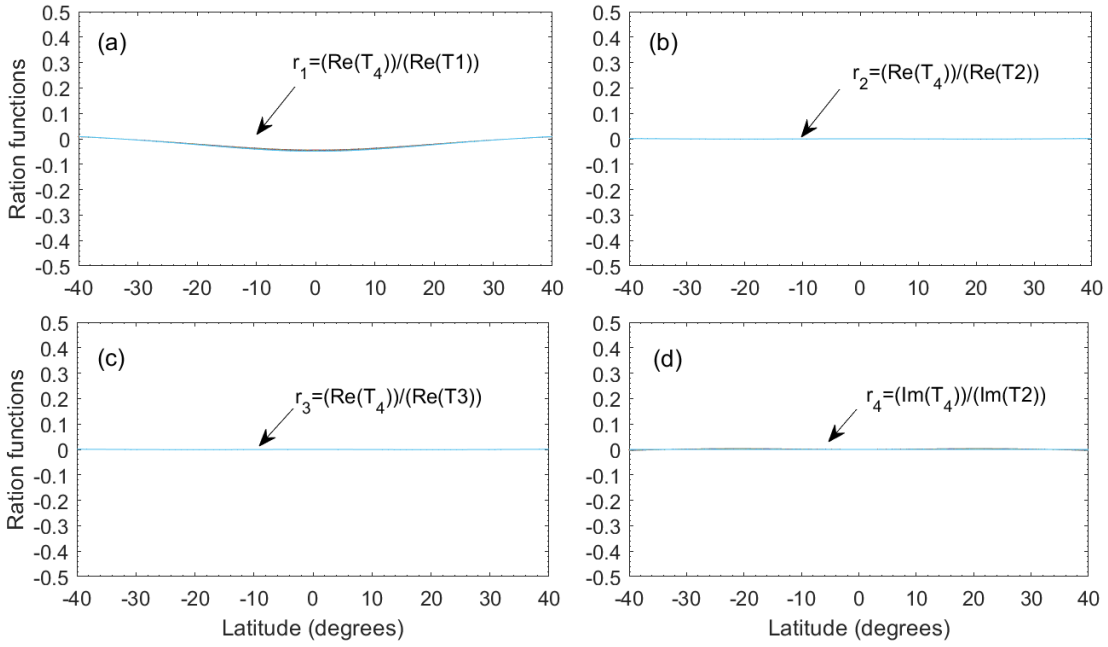

Figure A1. Ratio factor r_i vary with the latitude and relaxation τ. Here, N=10Ω, τ is set to be in the range of (2:0.1:20) yr. The results show that all the cases converge on one curve, indicating r_i is insensitive to the τ.

Defining $\mathrm{Z}(x) = \frac{C^2x^2}{M(x)} + \frac{mC}{M(x)} - M(x) - \frac{m^2}{1-x^2}$, which is further expressed by

$$\mathrm{Z}(x) = \underbrace{\left[\frac{C^2}{M(x)} - \beta^2 M(0)\right]}_{1} x^2 + \underbrace{\frac{mC}{M(x)} - M(0) - \frac{m^2}{1-x^2}}_{2} \tag{A9}$$

therefore, we will discuss the relationships between the following physical quantities

$$1)\ M(0)\ \text{and}\ \frac{mC}{M(x)};\ 2)\ \beta^2 M(0)\ \text{and}\ \frac{C^2}{M(x)}.$$

The expressions of the related quantities are written as

$$M(0) = \frac{V_a^2(0)k^4R^2(\omega^2+\alpha^2+\alpha\eta k^2)}{N^2[\omega^2+(\alpha+\eta k^2)^2]} - i\frac{V_a^2(0)k^6R^2\omega\eta}{N^2[\omega^2+(\alpha+\eta k^2)^2]} \tag{A10}$$

$$\frac{mC}{M(x)} = \frac{2\Omega m}{V_a^2k^2}\omega + i\frac{2\Omega m}{V_a^2k^2}(\alpha+\eta k^2) \tag{A11}$$

$$\frac{C^2}{M(x)} = \frac{4\Omega^2R^2}{V_a^2N^2}\chi\tilde{\omega}^2 = \frac{4\Omega^2R^2}{V_a^2N^2}[\omega^2 - \alpha(\alpha+\eta k^2)] + i\frac{4\Omega^2R^2\omega}{V_a^2N^2}(2\alpha+\eta k^2) \tag{A12}$$

Figure A2 shows the relationship between $M(0)$ and $\frac{mC}{M(x)}$ (here, taking H=20km, 25km, 30km, 35km, for examples). Figure A2(a) displays that the value of ratio (i.e., $\frac{Re(M(0))}{Re(\frac{mC}{M(x)})}$) changes with H and τ, which shows that the bigger the H value is, the smaller the ratio value is, here $\left|\frac{Re(M(0))}{Re(\frac{mC}{M(x)})}\right|$ <10^{-3} is obtained, so $|Re(M(0))| \ll \left|Re(\frac{mC}{M(x)})\right|$. Figure A2(b) displays the value of $\frac{Im(M(0))}{Im(\frac{mC}{M(x)})}$, which shows that the singularity phenomenon appears, which is due to $Im(\frac{mC}{M(x)})$=0

(when $\alpha + \eta k^2 = 0$). Therefore, to obtain $M(x) \ll \frac{mC}{M(x)}$, we must require $\alpha \neq -\eta k^2$, i.e., γ in formula (22) is required to $\gamma \neq 1$.

Figure A3 shows the ratio between the two quantities (i.e., $\beta^2 M(0)$ and $\frac{C^2}{M(x)}$), where, the ratios of the real parts (i.e., $\frac{Re(\beta^2 M(0))}{Re(\frac{C^2}{M(x)})}$) are shown in Figure A3(a), in general, the bigger H is, the smaller of the ratio value is, here, $\left|\frac{Re(\beta^2 M(0))}{Re(\frac{C^2}{M(x)})}\right| < 10^{-3}$ is obtained, therefore, we have $|Re(\beta^2 M(0))| \ll \left|Re(\frac{C^2}{M(x)})\right|$. Figure A3(b) also shows that $\frac{Im(\beta^2 M(0))}{Im(\frac{C^2}{M(x)})}$ owns the singularity phenomenon, when $2\alpha + \eta k^2 = 0$. If the relation (i.e., $\beta^2 M(0) \ll \frac{C^2}{M(x)}$) holds, we require that $\alpha \neq -0.5\eta k^2$, i.e., γ in formula (22) is required to $\gamma \neq 0.5$.

Here, we can tentatively remove the $M(x)$ term from the formula (A8) to reproduce the formula (10), but the final results (i.e., the γ value) of this work must be tested to ensure that the above relationships (i.e., $|Im[M(0)]| \ll \left|Im[\frac{mC}{M(x)}]\right|$ and $|Im[M(0)\beta^2]| \ll \left|Im\left[\frac{C^2}{M(x)}\right]\right|$, the proof of which is shown in discussion part of this work, see the relationship 2) are valid.

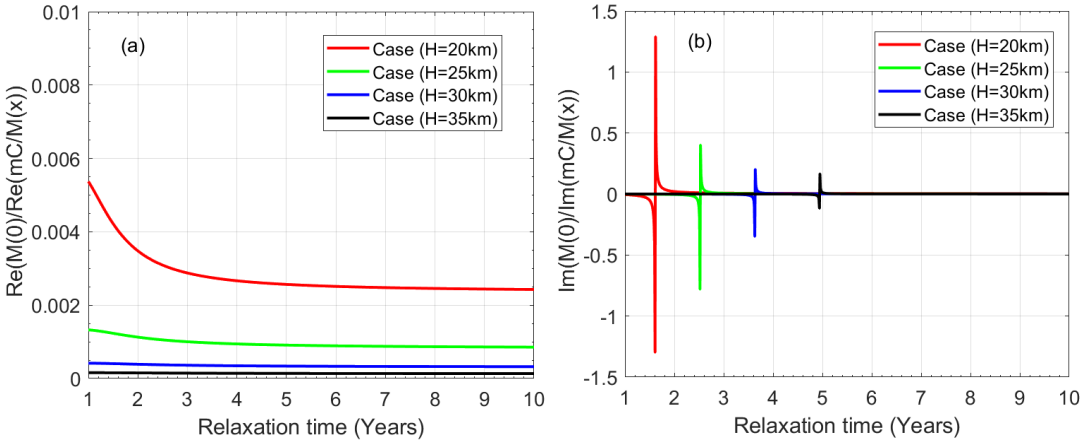

Figure A2. Comparison between $M(0)$ and $\frac{mC}{M(x)}$. (a) indicates that $Re(M(0)) \ll Re(\frac{mC}{M(x)})$; (b) shows that the ratio of $\frac{Im(M(0))}{Im(\frac{mC}{M(x)})}$ has the singularity points.

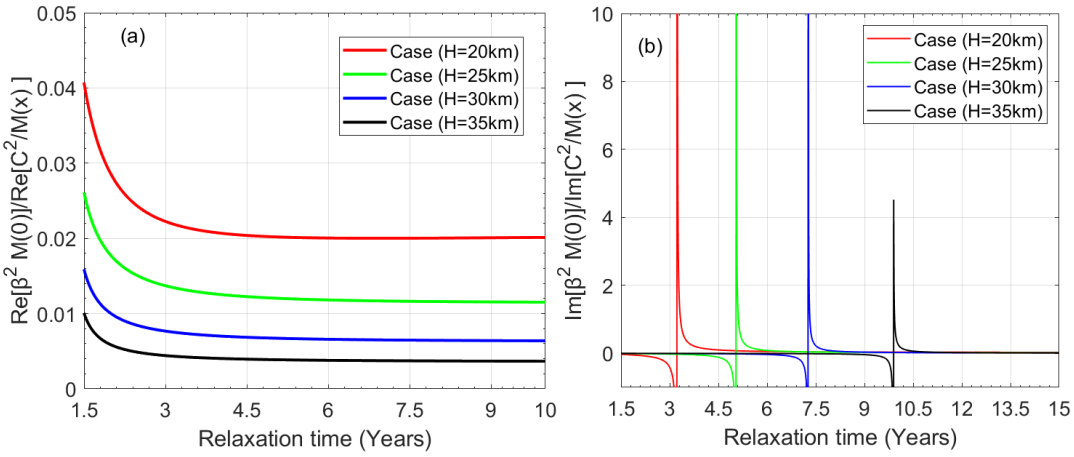

990

991 **Figure A3.** Comparison between $M(0)$ and $\frac{mC}{M(x)}$. (a) refers to the value of $\frac{Re(\beta^2 M(0))}{Re(\frac{C^2}{M(x)})}$; (b) shows the value of

992 $\frac{Im(\beta^2 M(0))}{Im(\frac{C^2}{M(x)})}$.

993

994 **Appendix B: On the derivation of 'Weber equation'.**

995 Here, we will show the derivation process of the 'Weber equation' (i.e., the equation (12)).

996 Taking $y(x) = \sqrt{(1-x^2)(1+\beta^2 x^2)}\tilde{b}'_\theta(x)$ into the equation (10), we can get

997 $$(1-x^2)\frac{\partial^2 y}{\partial x^2} + \left[\frac{(\beta^2 x - x - 2\beta^2 x^3)^2 - h^2(\beta^2 - 1 - 6\beta^2 x^2)}{h^2(1+\beta^2 x^2)} + \frac{C^2 x^2}{M(x)} + \frac{mC}{M(x)} - \frac{m^2}{1-x^2}\right] y = 0 \qquad \text{(B1)}$$

998 where, $h = \sqrt{(1-x^2)(1+\beta^2 x^2)}$, $M(x) = M(0)(1+\beta^2 x^2)$.

999 Furthermore, we have

1000 $$\frac{\partial^2 y}{\partial x^2} + \{\underbrace{\frac{(\beta^2 x - x - 2\beta^2 x^3)^2 - h^2(\beta^2 - 1 - 6\beta^2 x^2)}{(1-x^2)^2(1+\beta^2 x^2)^2}}_{\widetilde{T_1}} + \underbrace{\left[\frac{C^2 x^2}{M(0)} + \frac{mC}{M(0)}\right]\frac{1}{h^2}}_{\widetilde{T_2}} + \underbrace{\left[-\frac{m^2}{(1-x^2)^2}\right]}_{\widetilde{T_3}}\} y = 0 \qquad \text{(B2)}$$

1001 Defining

1002 $\widetilde{T_1} = \frac{(\beta^2 x - x - 2\beta^2 x^3)^2 - h^2(\beta^2 - 1 - 6\beta^2 x^2)}{(1-x^2)^2(1+\beta^2 x^2)^2} = \frac{(1-\beta^2) + 6\beta^2 x^2 + 3\beta^2(\beta^2 - 1)x^4 - 2\beta^4 x^6}{(1-x^2)^2(1+\beta^2 x^2)^2}$;

1003 $\widetilde{T_2} = \left[\frac{C^2 x^2}{M(0)} + \frac{mC}{M(0)}\right]\frac{1}{(1-x^2)(1+\beta^2 x^2)}$;

1004 $\widetilde{T_3} = -\frac{m^2}{(1-x^2)^2}$.

1005 This work mainly focuses on the equatorial regions. Considering $|\beta x| < 1$, that is $|x| < \frac{1}{\beta} <$

1006 1 (here β =1.58), so we can write the following expressions of series expansion

1007 $$\frac{1}{1-x^2} = (1+x^2) + \underbrace{x^4 + x^6 + \cdots}_{O(x^4)} \qquad \text{(B3)}$$

$$\frac{1}{1+\beta^2x^2} = (1-\beta^2x^2) + \underbrace{\beta^4x^4 - \beta^6x^6 + \cdots}_{O(x^4)} \quad \text{(B4)}$$

$$\frac{1}{(1-x^2)^2} = (1+2x^2) + \underbrace{3x^4 + 4x^6 + \cdots}_{O(x^4)} \quad \text{(B5)}$$

$$\frac{1}{(1+\beta^2x^2)^2} = (1-2\beta^2x^2) + \underbrace{3\beta^4x^4 - 4\beta^6x^6 + \cdots}_{O(x^4)} \quad \text{(B6)}$$

Focusing on the low-latitude regions to ensure that x is small enough. Removing the higher order terms (i.e., $O(x^4)$) from the above series, which is called as the truncation treatment, where changes of the related truncation errors with latitude are further shown in the supporting materials. Thus, we can write the following approximation expressions

$$\left.\begin{aligned} \widetilde{T_1} &= (1-\beta^2) + 2(\beta^4+\beta^2+1)x^2 + O(x^4) \\ \widetilde{T_2} &= [\tfrac{C^2}{M(0)} + \tfrac{mC}{M(0)}(1-\beta^2)]x^2 + \tfrac{mC}{M(0)} + O(x^4) \\ \widetilde{T_3} &= -(m^2 + 2m^2x^2) + O(x^4) \end{aligned}\right\} \quad \text{(B7)}$$

Then, the formula (B2) can be turned into

$$\partial_x^2 y + \{\underbrace{\left[\tfrac{mC}{M(0)} + 1 - \beta^2 - m^2\right] + \left[\tfrac{C^2}{M(0)} + \tfrac{mC}{M(0)}(1-\beta^2) + 2\beta^2(\beta^2+1) - 2(m^2-1)\right]x^2}_{remaining} + O(x^4)\} = 0 \quad \text{(B8)}$$

Furthermore, removing the term $O(x^4)$ from the formula (B8), and finally, we write the following simplified equation (i.e., the equation (12))

$$\frac{\partial^2 y}{\partial x^2} - (\alpha_0 x^2 - \alpha_1)y = 0$$

where, the two coefficients (i.e., α_0 and α_1) are respectively written as

$$\alpha_0 = -\frac{C^2}{M(0)} - \frac{mC}{M(0)}(1-\beta^2) - 2\beta^2(\beta^2+1) + 2(m^2-1);$$

$$\alpha_1 = \frac{mC}{M(0)} + 1 - \beta^2 - m^2.$$

Appendix C: On the perturbation analysis.

According to the above discussion, the derivation of the 'Weber equation' (i.e., the formula (12)) involves the so-called truncation treatment (i.e., removing the higher-order quantities expressed by $O(x^4)$), where the latitude is required to be low to guarantee that the truncation errors (due to removing $O(x^4)$) are small enough. Here, we will discuss the specific latitude range.

Defining the 'importance' of the $O(x^4)$ term with respect to the 'remaining' term in formula (B8) as

$$\Delta = abs\left(\frac{O(x^4)}{remaining}\right) = abs\left(\frac{B(x)}{A(x)}\right) \quad \text{(C1)}$$

where, 'abs' refers to the absolute value of the complex number; $B(x) = O(x^4) = \widetilde{T_1} + \widetilde{T_2} + \widetilde{T_3} - A(x)$; $A(x) = remaining$; the related expressions are further shown as follows

$\widetilde{T_1} = \frac{(1-\beta^2)+6\beta^2x^2+3\beta^2(\beta^2-1)x^4-2\beta^4x^6}{(1-x^2)^2(1+\beta^2x^2)^2}$;

$\widetilde{T_2} = [\frac{C^2x^2}{M(0)} + \frac{mC}{M(0)}]\frac{1}{(1-x^2)(1+\beta^2x^2)}$;

$\widetilde{T_3} = -\frac{m^2}{(1-x^2)^2}$;

$A(x) = \left[\frac{mC}{M(0)} + 1 - \beta^2 - m^2\right] + \left[\frac{C^2}{M(0)} + \frac{mC}{M(0)}(1-\beta^2) + 2\beta^2(\beta^2+1) - 2(m^2-1)\right]x^2$;

$C = \frac{2\Omega k^2R^2}{N^2}(\omega + i\alpha)$;

$M(0) = \frac{V_a^2(0)k^4R^2}{N^2[\omega^2+(\alpha+\eta k^2)^2]}[(\omega^2 + \alpha^2 + \alpha\eta k^2) - i\omega\eta k^2]$;

Furthermore, we can directly adopt the result (i.e., $\alpha \approx -\eta k^2$) of this work, then $M(0)$ can be further simplified as $M(0) = \frac{V_a^2(0)k^4R^2}{N^2}[1 - i\frac{\eta k^2}{\omega}]$.

Here, β=1.58, m=7, $\eta = \frac{1}{\mu\sigma}$, $\sigma = 10^6$S/m; $\omega = \frac{2\pi}{T}$, T =8.5yr; $k = \frac{\pi}{H}$, $V_a(0)$ =0.0048m/s. As for the stratification parameter values, we adopt N=10Ω (e.g., Knezek and Buffett, 2018) and take H=21km, 25km, 30km, 35km for examples. Thus, we can give the Δ values, see Figure A4, where the latitude is set to be within $\pm$30°. The results show that if the latitude is lower, the Δ value will be smaller, i.e., the importance of $O(x^4)$ with respect to the remaining term (in formula (B8)) will be weaker. When latitude is below 25 degrees, the Δ value will be smaller than ~0.1 (see Cases 1 and 2) and ~0.15 (see Cases 3 and 4). Moreover, when the latitude is less than 15° (i.e., the observed equatorial wave region reflected by the grey shadowed area displayed in Figure A4), the Δ value will be smaller than ~0.02.

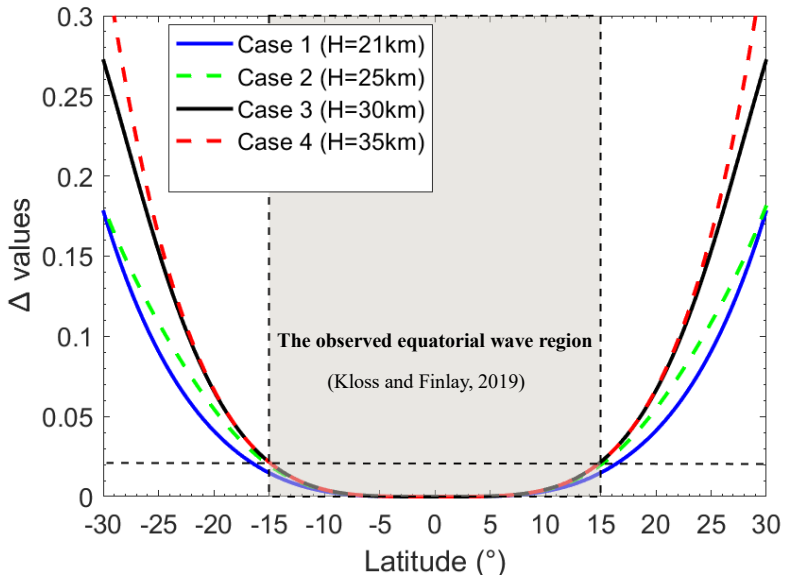

Figure A4. Variations of the Δ value with latitude and thickness *H*. The grey shadowed area (latitude below 15 degrees) indicates the region where the observed equatorial waves locate (Kloss and Finlay, 2019).

Here, a question arises: Whether it is reliable for 'Weber equation' (i.e., formula (12)) and its specific solution (i.e., formula (18)) to describe the properties of the equatorial waves (e.g., with latitude below 15°, see Kloss and Finlay, 2019). Here, we adopt the perturbation analysis approach to discuss it. Based on the above discussion, the formula (B8) can be further expressed by

$$\frac{\partial^2 y}{\partial x^2} + [A(x) + B(x)]y = 0 \tag{C2}$$

where, $A(x) = \alpha_1 - \alpha_0 x^2$ (see Appendix B); $B(x) = O(x^4)$ (see formula (C1)).

Introducing a ratio factor $\varepsilon = \frac{B(x)}{A(x)}$, here ε is called as the perturbation factor and it is a small quantity relative to 1. Note that there is a slight difference between ε and Δ in definition, (i.e., $\Delta = abs(\varepsilon)$), while the ε value can be inferred from the Δ value. Moreover, due to $B(x) = \varepsilon A(x)$, the formula (C2) can be further written as the following equation

$$\frac{\partial^2 y}{\partial x^2} + [(1+\varepsilon)A(x)]y = \frac{\partial^2 y}{\partial x^2} - (\alpha_0' x^2 - \alpha_1')y = 0 \tag{C3}$$

where, $\alpha_0' = (1+\varepsilon)\alpha_0$, $\alpha_1' = (1+\varepsilon)\alpha_1$.

Differing from the formula (12) (i.e., $\frac{\partial^2 y}{\partial x^2} - (\alpha_0 x^2 - \alpha_1)y = 0$), formula (C3) includes the perturbation effect from ε. Because we mainly focus on the low-latitude regions, the ε value can be quite smaller than 1. Here, the specific solution to the equation (C3) is still written in terms of the same form as that of the formula (18) (i.e., $y_n(x) = A_n e^{-\frac{1}{2}\tilde{\alpha}^2 x^2} H_n(\tilde{\alpha}x)$), that is

$$\tilde{y}_n(x) = A'_n e^{-\frac{1}{2}(\tilde{\alpha}')^2 x^2} H_n(\tilde{\alpha}' x) \quad \text{(C4)}$$

where, $A'_n = \sqrt{\frac{\tilde{\alpha}'}{\sqrt{\pi} 2^n n!}}$, $\tilde{\alpha}' = (\alpha'_0)^{\frac{1}{4}}$, meanwhile, the α'_0 and α'_1 satisfy the following relationship, i.e., $\tilde{\eta}' = (\alpha'_0)^{-\frac{1}{2}} \alpha'_1 = 2n + 1$.

Comparing the formula (C4) with the formula (18), the relative errors of $\tilde{\alpha} (= \alpha_0^{\frac{1}{4}})$ is expressed by $\left|\frac{\tilde{\alpha} - \tilde{\alpha}'}{\tilde{\alpha}}\right|$. Therefore,

$$\left|\frac{\tilde{\alpha} - \tilde{\alpha}'}{\tilde{\alpha}}\right| = \frac{[(1+\varepsilon)^{\frac{1}{4}} - 1]\alpha_0^{\frac{1}{4}}}{\tilde{\alpha}} = (1+\varepsilon)^{\frac{1}{4}} - 1 \quad \text{(C5)}$$

Additionally, the relative errors of $\tilde{\eta} (= \alpha_0^{-\frac{1}{2}} \alpha_1)$ is written as follows

$$\left|\frac{\tilde{\eta} - \tilde{\eta}'}{\tilde{\eta}}\right| = (1 + \varepsilon)^{\frac{1}{2}} - 1 \quad \text{(C6)}$$

When ε=0.1, i.e., $\Delta = abs(\varepsilon)$ =0.1, corresponding to the latitudes 22°~25°, which can be inferred from Figure A4, at this moment, the relative errors for both $\tilde{\alpha}$ and $\tilde{\eta}$ are small: $\left|\frac{\tilde{\alpha} - \tilde{\alpha}'}{\tilde{\alpha}}\right|$ ~2.4% and $\left|\frac{\tilde{\eta} - \tilde{\eta}'}{\tilde{\eta}}\right|$ ~4.9%. Moreover, when latitude is lower, the ε value will be smaller, and the relative errors will be further weaker as well, e.g., when $\varepsilon \leq$0.02 (corresponding to the latitude below 15°, see Figure A4), then $\left|\frac{\tilde{\alpha} - \tilde{\alpha}'}{\tilde{\alpha}}\right| \leq 0.5\%$ and $\left|\frac{\tilde{\eta} - \tilde{\eta}'}{\tilde{\eta}}\right| \leq 1\%$.

Next, we will further discuss the relative errors of $y_n(x)$, which is expressed by

$$\epsilon_n = \left|\frac{y_n(x) - \tilde{y}_n(x)}{y_n(x)}\right| \quad \text{(C7)}$$

The results of ϵ_n (with degrees *n*=0,1,2,3) are displayed in Figure A5, which shows that ϵ_n values will decrease as the latitude is lower. Generally, if the latitude is below 25°, ϵ_n is shown to be less than 5% (expect the mode *n*=3, which reaches to 10%), while if the latitude is lower than 20°, the ϵ_n values (*n*=0,1,2) will be obviously smaller than 5%, except the mode *n*=3, whose relative errors yet exceeds 15%, which probably reflects the instability of the errors (for the higher degree modes) locating at the relatively larger latitude regions. Nevertheless, when the latitude is reduced to 15° (or smaller, e.g., 13°), the relative errors of all the modes are shown to be stable and quite small (i.e., < 3%).

In summary, the perturbation analysis indicates that, even though the perturbation factor ε value reaches to 0.1 (corresponding to the latitude 25°), the relative errors caused by the truncation treatment are still quite small (i.e., < 5%), and the relative errors will be further reduced as the

latitude is lower. Hence, the developed models and the related results of this work are reliable to study the observed low-latitude hydromagnetic waves and their related physical properties.

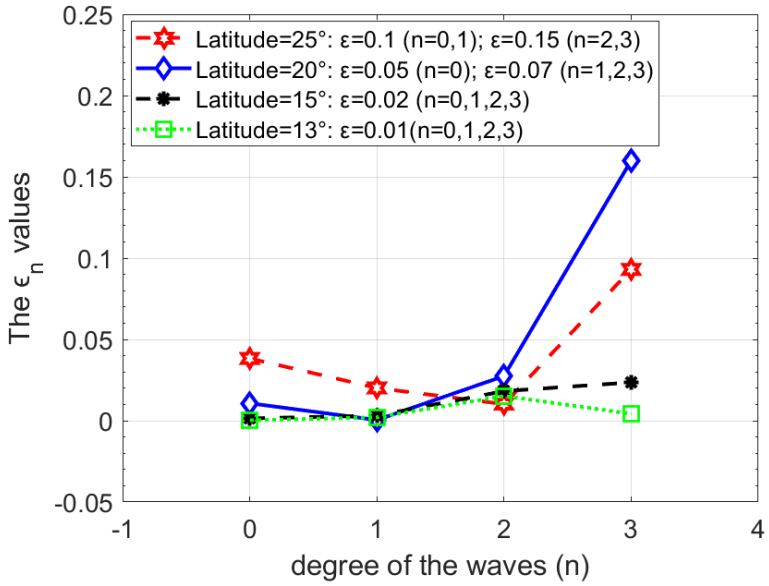

Figure A5. The relative errors of $y_n(x)$ change with the latitude and degree n.

Appendix D: Proof of the sufficient and necessary condition.

Here, we can prove that the expression (i.e., $\tilde{\eta}(=\alpha_0^{-\frac{1}{2}}\alpha_1) = 2n+1$) is the sufficient and necessary condition that the equation (15) owns the Hermite polynomial solution $H_n(\xi)$. Here the equation (15) is repeated as follows

$$H''(\xi) - 2\xi H'(\xi) + (\tilde{\eta} - 1)H(\xi) = 0 \tag{D1}$$

The Hermite polynomial solution (i.e., $H_n(\xi)$) is written as

$$H_n(\xi) = (-1)^n e^{\xi^2} \frac{d^n}{d\xi^n}(e^{-\xi^2})$$

In mathematics, $H_n(\xi)$ owns the following important recurrence relations ($n \geq 1$):

$$H_{n+1}(\xi) - 2\xi H_n(\xi) + 2nH_{n-1}(\xi) = 0 \tag{D2}$$

$$H_n{}'(\xi) = 2nH_{n-1}(\xi) \tag{D3}$$

1) Proof of the necessity

If the expression (i.e., $\tilde{\eta}(=\alpha_0^{-\frac{1}{2}}\alpha_1) = 2n+1$) is valid, then the equation (D1) can be expressed by

$$H''(\xi) - 2\xi H'(\xi) + 2nH(\xi) = 0 \tag{D4}$$

Thus, we need to prove that $H_n(\xi)$ is the solution to the equation (D4).

According to the formula (D2), we can give that ($n \geq 2$)

$$H_n(\xi) - 2\xi H_{n-1}(\xi) + 2(n-1)H_{n-2}(\xi) = 0 \quad \text{(D5)}$$

Using the formula (D3), we have ($n \geq 2$)

$$H_n''(\xi) = 2nH'_{n-1}(\xi) = 4n(n-1)H_{n-2}(\xi) \quad \text{(D6)}$$

Taking $H_n(\xi)$, $H_n'(\xi)$ and $H_n''(\xi)$ into the left hand of the equation (D4), and considering the formulas (D3), (D5) and (D6), we can obtain ($n \geq 2$)

$$H_n''(\xi) - 2\xi H_n'(\xi) + 2nH_n(\xi) = 2n[H_n(\xi) - 2\xi H_{n-1}(\xi) + 2(n-1)H_{n-2}(\xi)] = 0$$

Furthermore, considering the cases of n=0 and 1 respectively as follows:

when $n = 0$, $H_0(\xi)$=1, so $H_0''(\xi) - 2\xi H_0'(\xi) + 2 \cdot 0 \cdot H_0(\xi) = 0$;

when $n = 1$, $H_1(\xi)$=2ξ, so $H_1''(\xi) - 2\xi H_1'(\xi) + 2 \cdot 1 \cdot H_1(\xi) = -4\xi + 4\xi = 0$.

To summarize, $n \geq 0$, we have $H_n''(\xi) - 2\xi H_n'(\xi) + 2nH_n(\xi) = 0$.

Therefore, the necessity is proved.

2) Proof of the sufficiency

If the equation (D1) owns the Hermite polynomial solution (i.e., $H_n(\xi)$), then $H_n(\xi)$ satisfies

$$H_n''(\xi) - 2\xi H_n'(\xi) + (\tilde{\eta} - 1)H_n(\xi) = 0 \quad \text{(D7)}$$

Here, we need to prove that $\tilde{\eta} = 2n + 1$ (alternatively $\alpha_1 = (2n+1)\sqrt{\alpha_0}$) is valid.

Taking the formulas (D3) and (D6) into the formula (D7), we can obtain

$$(\tilde{\eta} - 1)H_n(\xi) - 4n[\xi H_{n-1}(\xi) - (n-1)H_{n-2}(\xi)] = 0 \quad \text{(D8)}$$

Using the formula (D2) or the formula (D5), we have

$$\xi H_{n-1}(\xi) - (n-1)H_{n-2}(\xi) = \frac{1}{2}H_n(\xi) \quad \text{(D9)}$$

Taking the formula (D9) into the formula (D8), we have

$$(\tilde{\eta} - 1 - 2n)H_n(\xi) = 0 \quad \text{(D10)}$$

Here, $H_n(\xi) \neq 0$, so $\tilde{\eta}(= \alpha_0^{-\frac{1}{2}}\alpha_1) = 2n + 1$, that is $\alpha_1 = (2n+1)\sqrt{\alpha_0}$.

Therefore, the sufficiency is proved.

Appendix E: Proof of the specific solution to the equation (12).

According to the formula (18)

$$y(x) = A_n e^{-\frac{1}{2}\tilde{\alpha}^2 x^2} H_n(\tilde{\alpha}x)$$

Here, $H_n(\xi)$ is the Hermite polynomial, which satisfies the following Hermite differential equation

$$H_n''(\xi) - 2\xi H_n'(\xi) + 2nH_n(\xi) = 0 \quad \text{(E1)}$$

The second-order partial derivative of $y(x)$ is written as

$$\frac{\partial^2 y}{\partial^2 x} = A_n\tilde{\alpha}^2 e^{-\frac{1}{2}\tilde{\alpha}^2x^2}[H_n''(\tilde{\alpha}x) - 2\tilde{\alpha}xH_n'(\tilde{\alpha}x) + (\tilde{\alpha}^2x^2 - 1)H_n(\tilde{\alpha}x)] \quad \text{(E2)}$$

Here, $\tilde{\alpha} = \alpha_0^{\frac{1}{4}}$ and $\tilde{\eta} = \alpha_0^{-\frac{1}{2}}\alpha_1 = 2n + 1$, so we obtain $\alpha_0 = \tilde{\alpha}^4$ and $\alpha_1 = \sqrt{\alpha_0}\tilde{\eta} = \tilde{\eta}\tilde{\alpha}^2$. We can write the following formula

$$\frac{\partial^2 y}{\partial x^2} - (\alpha_0x^2 - \alpha_1)y = A_n\tilde{\alpha}^2 e^{-\frac{1}{2}\tilde{\alpha}^2x^2}[H_n''(\tilde{\alpha}x) - 2\tilde{\alpha}xH_n'(\tilde{\alpha}x) + (\tilde{\eta} - 1)H_n(\tilde{\alpha}x)]$$

$$= A_n\tilde{\alpha}^2 e^{-\frac{1}{2}\tilde{\alpha}^2x^2}[H_n''(\tilde{\alpha}x) - 2\tilde{\alpha}xH_n'(\tilde{\alpha}x) + 2nH_n(\tilde{\alpha}x)] \quad \text{(E3)}$$

where, $\xi = \tilde{\alpha}x$.

Thus, we have

$$\frac{\partial^2 y}{\partial x^2} - (\alpha_0x^2 - \alpha_1)y = A_n\tilde{\alpha}^2 e^{-\frac{1}{2}\xi^2}[H_n''(\xi) - 2\xi H_n'(\xi) + 2nH_n(\xi)]=0$$

Therefore, $y(x) = A_n e^{-\frac{1}{2}\tilde{\alpha}^2x^2}H_n(\tilde{\alpha}x)$ is proved to be the specific solution of equation (12), where, the existence condition of this specific solution is that these two coefficients (i.e., α_0 and α_1) satisfy $\alpha_1 = (2n + 1)\sqrt{\alpha_0}$.

References

Aubert, J., & Finlay, C.C. 2019. Geomagnetic jerks and rapid hydromagnetic waves focusing at Earth's core surface. Nature Geoscience, 12, 393-398.

Bergman, M.I.,1993. Magnetic Rossby waves in a stably stratified layer near the surface of the Earth's outer core, Geophys. Astrophys. Fluid Dyn., 68, 151–176.

Braginsky, S.,1993. MAC oscillations of the hidden ocean of the core, J. Geomag. Geoelectr.,48,1517–1538.

Buffett, B. A., 2014. Geomagnetic fluctuations reveal stable stratification at the top of the Earth's core. Nature. 507. doi:10.1038/nature13122.

Buffett, B. A. & Knezek, N. 2018. Stochastic generation of MAC waves and implications for convection in Earth's core. Geophys. J. Int. 212, 1523-1535.

Buffett, B.A. & Matsui, H. 2019. Equatorially trapped waves in Earth's core. Geophys. J. Int. 218, 1210-1225.

Buffett, B.A. & Seagle, C.T., 2010. Stratification of the top of the core due to chemical interactions with the

mantle. J. Geophys. Res: Solid Earth, 115, B04407, doi:10.1029/2009JB006751.

Chi-Durán, R., Avery, M.S., Knezek, N. & Buffett, B.A. 2020. Decomposition of geomagnetic secular Acceleration into traveling waves using complex empirical orthogonal functions. Geophys. Res. Lett., 47, https://doi.org/10.1029/2020gl087940.

Christensen, U.R. 2018. Geodynamo models with a stable layer and heterogeneous heat flow at the top of the core. Geophys. J. Int. 215,1338-1351.

Christensen, U.R. & Aubert, J., 2006. Scaling properties of convection driven dynamos in rotating spherical shells and application to planetary magnetic fields. Geophys. J. Int., 166, 97–114.

Chulliat, A., Thebault, E. & Hulot, G., 2010. Core field acceleration pulse as a common cause of the 2003 and 2007 geomagnetic jerks, Geophys. Res. Lett., 37(7), doi:10.1029/2009GL042019.

Chulliat, A., Alken, P. & Maus, S. 2015. Fast equatorial waves propagating at the top of the Earth's core. Geophys. Res. Lett., 42,3321-3329.

Chulliat, A. & Maus, S. 2014.Geomagnetic secular acceleration, jerks, and localized standing waves at the core surface from 2000 to 2010. J. Geophys. Res: Solid Earth, 119,1531-1543.

Duan, P. S. & Huang, C. L. 2020. Intradecadal variations in length of day and their correspondence with geomagnetic jerks. Nature Communications. https://doi.org/10.1038 /s41467-020-16109-8.

Finlay, C.C., Dumberry, M., Chulliat, A. &Pais, M.A. 2010. Short timescale core dynamics: theory and observations. Space Sci Rev, 155:177-218.

Finlay, C.C., Olsen, N. & Kotsiaros, S., et al. 2016. Recent geomagnetic secular variation from Swarm and ground observatories as estimated in the CHAOS-6 geomagnetic field model. Earth Planets Space. 68:112, doi: 10.1186/s40623-016-0486-1.

Finlay, C.C. & Jackson, A.,2003. Equatorially dominated magnetic field change at the surface of Earth's core. Science,300 (5628),2084-2086.

Gastine, T., Aubert, J. & Fournier, A.,2019. Dynamo-based limit to the extent of a stable layer atop Earth's core. Geophys. J. Int., 200, 1-16.

Gerick, F., Jault, D. & Noir, J., 2020. Fast quasi-geostrophic Magneto-Coriolis modes in the Earth's core. Geophys. Res. Lett., doi:10.1029/2020GL090803.

Gilbert, F., 1970. Excitation of the normal modes of the Earth by earthquake sources. Geophys. J. R. Astr. Soc. 22, 223-226.

1205 Gillet, N., Gerick, F., Angappan, R and Jault, D. 2021. A dynamical prospective on interannual geomagnetic field
1206 changes. Surveys in Geophysics. https://doi.org/10.1007/s10712-021-09664-2.
1207 Gillet, N., Jault, D. & Finlay, C. C. 2015. Planetary gyre, time-dependent eddies, torsional waves and
1208 Equatorial jets at the Earth's core surface, J. Geophys. Res: Solid Earth. 120, 3991-4013, doi:10.1002/
1209 2014JB011786.
1210 Gillet, N., Schaeffer, N. &Jault, D. 2012. Rationale and geophysical evidence for quasi-geostrophic rapid
1211 dynamics within the Earth's outer core. Phys. Earth Planet. Inter. 202-203:78-88.
1212 Gillet, N., Gerick, F., Jault, D., Schwaiger, T., Aubert, J., Istas, M. 2022. Satellite magnetic data reveal interannual
1213 waves in Earth's core. Proc. Natl Acad.Sci.1-7.
1214 Gubbins, D. & Davies, C. J., 2013. The stratified layer at the core-mantle boundary caused by barodiffusion of
1215 oxygen, sulphur and silicon. Phys. Earth Planet. Inter. 215: 21-28.
1216 Helffrich, G. & Kaneshima, S., 2010. Outer-core compositional stratification from observed core wave speed
1217 profile. Nature. 468:807-810.
1218 Hsu, C.C., Duan, P.S., Xu, X.Q., Zhou, Y.H. & Huang, C.L., 2021. On the ~7 year periodic signal in length of day
1219 from a frequency domain stepwise regression method. J. Geodesy, 95:55, https://doi.org/10.1007
1220 /s00190-021-01503-x.
1221 Jackson, A. 2003. Intense equatorial flux spots on the surface of the Earth's core. Nature. 424: 760-763.
1222 Kloss, C. & Finlay, C. 2019. Time-dependent low-latitude core flow and geomagnetic field acceleration pulses.
1223 Geophys. J. Int. 217, 140-168.
1224 Knezek, N. & Buffett, B., 2018. Influence of magnetic field configuration on magnetohydrodynamic waves in
1225 Earth's core. Phys. Earth Planet. Inter., 227:1-9.
1226 Knezek, N. & Buffett, B., 2019. Extracting waves from noisy geomagnetic data - A synthetic study of equatorially
1227 trapped waves in Earth's core. Phys. Earth Planet. Inter., 286: 81-91.
1228 Mandea, M., Holme, R., Pais,A., Pinheiro, K., Jackson, A. & Verbanac, G. 2010. Geomagnetic jerks: Rapid core
1229 field variations and core dynamics. Space. Sci. Rev., 155:147-175.
1230 Ohta, K., Kuwayama, Y., Hirose, K., Shimizu, K., & Ohishi, Y., 2016. Experimental determination of the electrical
1231 resistivity of iron at Earth's core conditions. Nature. 534, 95-98.
1232 Teed, R.J., Jones, C.A., & Tobias, S.M., 2019. Torsional waves driven by convection and jets in Earth's liquid core.
1233 Geophys J Int, 216, 123-129.
1234 Vidal, J., & Schaeffer, N., 2015. Quasi-geostrophic modes in the Earth's fluid core with an outer stably stratified

1235 layer. Geophys. J. Int., 202, 2182-2193.

1236 Wardinski, I., Holme, R., Asari, S.& Mandea, M., 2008. The 2003 geomagnetic jerks and its relation to the core

1237 surface flows, Earth Planet. Sci. Lett., 267(3-4), 468-481.

Supplementary Materials

1）On the derivation process of the equation (A1)

Here, we have the following formula (S1), i.e., the formula (8) in the manuscript.

$$\left.\begin{array}{c}\partial_x^2\tilde{b}'_\theta-\frac{M(x)}{1-x^2}\tilde{b}'_\theta=Cxi\tilde{b}'_\varphi+im\partial_x\tilde{b}'_\varphi\\ \tilde{b}'_\varphi=\frac{Cxi\tilde{b}'_\theta-im\partial_x\tilde{b}'_\theta}{m^2+(1-x^2)M(x)}\end{array}\right\} \tag{S1}$$

where, $M(x)=M(0)(1+\beta^2x^2)$.

Defining $f=m^2+(1-x^2)M(x)$, so we have

$$\tilde{b}'_\varphi=\frac{Cxi\tilde{b}'_\theta-im\partial_x\tilde{b}'_\theta}{f} \tag{S2}$$

Furthermore, we can obtain the first-order derivative of f, which is expressed as

$$\partial_x f=-2xM(x)+(1-x^2)\partial_x M(x)=2x(\beta^2-1-2\beta^2x^2)M(0) \tag{S3}$$

So, we can get

$$\partial_x\tilde{b}'_\varphi=\frac{f\partial_x\left(Cxi\tilde{b}'_\theta-im\partial_x\tilde{b}'_\theta\right)-(Cxi\tilde{b}'_\theta-im\partial_x\tilde{b}'_\theta)\partial_x f}{f^2}=\frac{\left(Ci\tilde{b}'_\theta+Cxi\partial_x\tilde{b}'_\theta-im\partial_x^2\tilde{b}'_\theta\right)f-(Cxi\tilde{b}'_\theta-im\partial_x\tilde{b}'_\theta)\partial_x f}{f^2}$$

Taking the formulas(S2) and (S3) into the formula (S1), we have

$$\partial_x^2\tilde{b}'_\theta-\frac{M(x)}{1-x^2}\tilde{b}'_\theta=Cxi\frac{Cxi\tilde{b}'_\theta-im\partial_x\tilde{b}'_\theta}{f}+im\frac{\left(Ci\tilde{b}'_\theta+Cxi\partial_x\tilde{b}'_\theta-im\partial_x^2\tilde{b}'_\theta\right)f+(im\partial_x\tilde{b}'_\theta-Cxi\tilde{b}'_\theta)\partial_x f}{f^2} \tag{S4}$$

so

$$\partial_x^2\tilde{b}'_\theta-\frac{M(x)}{1-x^2}\tilde{b}'_\theta=\frac{1}{f}m^2\partial_x^2\tilde{b}'_\theta-\frac{\partial_x f}{f^2}m^2\partial_x\tilde{b}'_\theta+(\frac{\partial_x f}{f^2}Cmx-\frac{C^2}{f}x^2-\frac{Cm}{f})\tilde{b}'_\theta \tag{S5}$$

Furthermore

$$\left(1-\frac{m^2}{f}\right)\partial_x^2\tilde{b}'_\theta+\frac{\partial_x f}{f^2}m^2\partial_x\tilde{b}'_\theta+\left(\frac{C^2}{f}x^2+\frac{Cm}{f}-\frac{M(x)}{1-x^2}-\frac{\partial_x f}{f^2}Cmx\right)\tilde{b}'_\theta=0$$

so

$$(f-m^2)\partial_x^2\tilde{b}'_\theta+\frac{\partial_x f}{f}m^2\partial_x\tilde{b}'_\theta+\left(C^2x^2+Cm-\frac{M(x)}{1-x^2}f-\frac{\partial_x f}{f}Cmx\right)\tilde{b}'_\theta=0 \tag{S6}$$

That is

$$(1-x^2)M(x)\partial_x^2\tilde{b}'_\theta+2x(\beta^2-1-2\beta^2x^2)M(0)\frac{m^2}{f}\partial_x\tilde{b}'_\theta+\Big(C^2x^2+Cm-\frac{M(x)}{1-x^2}f-$$

$$\frac{2x(\beta^2-1-2\beta^2x^2)M(0)}{f}Cmx\Big)\tilde{b}'_\theta=0$$

So, we have

$$(1-x^2)\partial_x^2\tilde{b}'_\theta-\frac{2x(1-\beta^2+2\beta^2x^2)}{1+\beta^2x^2}\frac{m^2}{f}\partial_x\tilde{b}'_\theta+\left(\frac{C^2x^2}{M(x)}+\frac{Cm}{M(x)}-\frac{f}{1-x^2}-\frac{2m(\beta^2-1-2\beta^2x^2)x^2}{(1+\beta^2x^2)}\frac{C}{f}\right)\tilde{b}'_\theta=0$$

Finally, we derive the following equation, i.e., the equation (A1) in the manuscript.

$$(1-x^2)\partial_x^2\tilde{b}'_\theta - \frac{2x(1-\beta^2+2\beta^2x^2)}{1+\beta^2x^2}\frac{m^2}{f}\partial_x\tilde{b}'_\theta + \left(\frac{C^2x^2}{M(x)} + \frac{Cm}{M(x)} - \frac{m^2}{1-x^2} - M(x) + \frac{2m(1-\beta^2+2\beta^2x^2)x^2}{(1+\beta^2x^2)}\frac{C}{f}\right)\tilde{b}'_\theta = 0 \quad \text{(S7)}$$

2) The truncation error analysis

$$\frac{1}{1-x^2} = \underbrace{1+x^2}_{remaining} + \underbrace{x^4+x^6+\cdots}_{O(x^4)} \quad \text{(S8)}$$

$$\frac{1}{1+\beta^2x^2} = \underbrace{1-\beta^2x^2}_{remaining} + \underbrace{\beta^4x^4-\beta^6x^6+\cdots}_{O(x^4)} \quad \text{(S9)}$$

$$\frac{1}{(1-x^2)^2} = \underbrace{1+2x^2}_{remaining} + \underbrace{3x^4+4x^6+\cdots}_{O(x^4)} \quad \text{(S10)}$$

$$\frac{1}{(1+\beta^2x^2)^2} = \underbrace{1-2\beta^2x^2}_{remaining} + \underbrace{3\beta^4x^4-4\beta^6x^6+\cdots}_{O(x^4)} \quad \text{(S11)}$$

where, β =1.58.

Defining the following residual series:

$$Res_1 = \underbrace{\frac{1}{1-x^2}}_{O_1} - \underbrace{(1+x^2)}_{remaining} = x^4+x^6+\cdots;$$

$$Res_2 = \underbrace{\frac{1}{1+\beta^2x^2}}_{O_2} - \underbrace{(1-\beta^2x^2)}_{remaining} = \beta^4x^4-\beta^6x^6+\cdots;$$

$$Res_3 = \underbrace{\frac{1}{(1-x^2)^2}}_{O_3} - \underbrace{(1+2x^2)}_{remaining} = 3x^4+4x^6+\cdots;$$

$$Res_4 = \underbrace{\frac{1}{(1+\beta^2x^2)^2}}_{O_4} - \underbrace{(1-2\beta^2x^2)}_{remaining} = 3\beta^4x^4-4\beta^6x^6+\cdots;$$

where, O_i (i=1,2,3,4) refers to the i_{th} original term.

Consequently, the relative errors are expressed by

$$\epsilon_i = \left|\frac{Res_i}{O_i}\right| \quad \text{(S12)}$$

The result is shown in the Figure S1

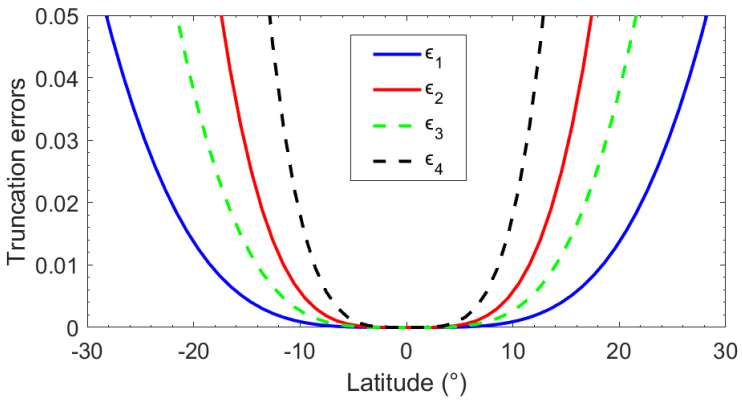

Figure S1. The truncation errors change with latitude ($\epsilon_i \leq 0.05$ is shown)